HLA-E and NKG2A Mediate Resistance to BCG Immunotherapy in Non-Muscle-Invasive Bladder Cancer

D. Ranti[1,2,3,4,5*], H. Yu[1,2,3,4*], B. Salomé[1,2,3,4,*], S. Bang[6], I. Duquesne[1,2,3,4,5], Y.A. Wang[1,2,3,4,5], C. Bieber[1,2,3,4,5], T. Strandgaard[7,8], E. Merritt[3,6], G. Doherty[9,10], A. Narasimhan[9,10], I. Okulate[1,2,3,4], Sean Houghton[11], B. Hug[1,2,3,4,5], J. Kim[11], H. Ravichandran[11], A. Demetriou[1,2,3,4,5], Z. Li[1,2,3,4,9], S. V. Lindskrog[7,8], A. N. M. Rangel da Silva[1,2,3,4,12], D.F. Ruan[1,2,3,4], J. Daza[1,2,3,4,5], J. Cris Ingles[1,2,3,4], R. Rai[4], E. Hegewisch-Solloa[13], E.M. Mace[13], R. Fernandez-Rodriguez[2,4], S. Izadmehr[4,9], A.M. Farkas[3,4,9], P. Cruz-Encarnacion[1,2], S. Shroff[6,14], F. Patel[3,15], M. Tran[3,4,9], D. Youssef[3,4,9], A. Ananthanarayanan[3,4,9] J. Park[1,2,3,4], D. Geanon[16], G. Kelly[16], B. Lee[16], K. Nie[16], S. Miake-Lye[16], H. Xie[16], R. Chen[16], C. Bi[16], T. Rizakos[16], B. Villagomez[16], T.H. Thin[17], M. Garcia-Barros[17], H. Brown[17], B. Martin[17], A. Mateo[17], A. Soto[17], R. Sussman[17], S. Shiwlani[17], S. Francisco-Simon[17], K.G. Beaumont[6,14], Y-C. Wang[6,14], L. Wang[9], R.P. Sebra[6,14,18], S. Smith[19], M. Skobe[2,4], E. Clancy-Thompson[20], D. Palmer[20], S. Hammond[20], P. Yolmo[21]; M. Koti[21], B. D. Hopkins[11], P. Wiklund[5], J. Zhu[6,14], J.J. Bravo-Cordero[9,10], R. Brody[17], Z. Chen[1,3,16], S. Kim-Schulze[1,3,16], L. Dyrskjøt[7,8], O. Elemento[11], A. Tocheva[3,6], W-M. Song[6], N. Bhardwaj[3,4,9], M.D. Galsky[4,9], J.P. Sfakianos[5#] & A. Horowitz[1,2,3,4#]

[1]Department of Immunology and Immunotherapy, Icahn School of Medicine at Mount Sinai, New York, NY, USA
[2]Department of Oncological Sciences, Icahn School of Medicine at Mount Sinai, New York, NY, USA
[3]The Marc and Jennifer Lipschultz Precision Immunology Institute, Icahn School of Medicine at Mount Sinai, New York, NY, USA
[4]Tisch Cancer Institute, Icahn School of Medicine at Mount Sinai, New York, NY, USA
[5]Department of Urology, Icahn School of Medicine at Mount Sinai, New York, NY, USA
[6]Department of Genetics and Genomic Sciences, Icahn School of Medicine at Mount Sinai, New York, NY, USA
[7]Department of Molecular Medicine, Aarhus University Hospital, Aarhus, Denmark
[8]Department of Clinical Medicine, Aarhus University, Aarhus, Denmark
[9]Division of Hematology and Medical Oncology, Department of Medicine, Icahn School of Medicine at Mount Sinai, New York, NY, USA
[10]Microscopy and Advanced Bioimaging Core, Icahn School of Medicine at Mount Sinai, New York, NY, USA
[11]Caryl and Israel Englander Institute for Precision Medicine, Weill Cornell Medicine, New York, NY, USA
[12]Laboratory of Virology, Institute of Biological Sciences, Federal University of Pará, Belém, Pará, Brazil
[13]Department of Pediatrics, Vagelos College of Physicians and Surgeons, Columbia University, New York NY, USA
[14]Icahn Institute for Data Science and Genomics Technology, Icahn School of Medicine at Mount Sinai, New York, NY, USA

[15]Department of Microbiology, Icahn School of Medicine at Mount Sinai, New York, NY, USA
[16]Human Immune Monitoring Center, Icahn School of Medicine at Mount Sinai, New York, NY, USA
[17]Department of Pathology, Molecular and Cell-Based Medicine, Icahn School of Medicine at Mount Sinai, New York, NY
[18]Black Family Stem Cell Institute, Icahn School of Medicine at Mount Sinai, New York, NY, USA
[19]Centre for Inflammation Research and Translational Medicine, Department of Biosciences, Brunel University of London, London, UK
[20]AstraZeneca, Oncology R & D Unit, Gaithersburg, Maryland, USA
[21]Department of Biomedical and Molecular Sciences, Cancer Research Institute, Queen's University, Kingston, ON, CANADA
* These authors contributed equally
# Co-Senior author

Running title. HLA-E and NKG2A in BCG Resistance

Keywords. Non-muscle-invasive bladder cancer; BCG-unresponsive; NK cells; Immunotherapy.

Corresponding Authors:
Amir Horowitz, PhD
Associate Professor of Immunology & Immunotherapy and Oncological Sciences
Lipschultz Precision Immunology Institute and Tisch Cancer Institute
Icahn School of Medicine at Mount Sinai
1425 Madison Ave., Box 1630
New York, New York 10029
Tel: (212) 659-9391 | Fax: (646) 537-9577
Email: amir.horowitz@mssm.edu

John P. Sfakianos, MD
Associate Professor of Urology
Icahn School of Medicine at Mount Sinai
1425 Madison Ave., L6-58, Box 1272
New York, New York 10029
Tel: (212) 659-9375
Email: john.sfakianos@mountsinai.org

Conflict of Interest Disclosure Statement: The authors declare no potential conflicts of interest.

Word Count (excluding methods and references): 6705

Fig. Count: 6

Table Count: 0

SUMMARY

Bacillus Calmette-Guérin (BCG) is the first-line therapy for high-grade non-muscle-invasive bladder cancer (NMIBC), yet many patients experience recurrence due to immune evasion. We identify HLA-E and NKG2A as mediators of adaptive resistance involving chronic activation of NK and T cells in BCG-unresponsive tumors. Prolonged IFN-γ exposure enhances HLA-E and PD-L1 expression on recurrent tumors, accompanied by the accumulation of NKG2A+ NK and CD8 T cells. HLA-E^{high} tumor cells preferentially cluster near CXCL12-rich stromal regions with dense effector cell presence, underscoring a spatially segregated tumor architecture. Although cytotoxic lymphocytes retain effector potential, their activity is restrained by HLA-E/NKG2A and PD-L1/PD-1 pathways located in their immediate neighborhood within the bladder tumor microenvironment. These data reveal a spatially organized immune escape program that limits anti-tumor immunity. Our findings support dually targeting NKG2A and PD-L1 checkpoint blockade as a rational, bladder-sparing strategy for patients with BCG-unresponsive NMIBC.

INTRODUCTION

In non-muscle-invasive bladder cancer (NMIBC), Bacillus Calmette-Guérin (BCG) remains the only FDA-approved frontline intravesical immunotherapy[1]. Upon transurethral resection of the bladder tumor (TURBT), BCG is administered weekly, intravesical, over six weeks as adjuvant therapy. BCG induces inflammation and IFN-γ production via recruitment and activation of multiple immune lineages, including monocytes, neutrophils, dendritic cells (DCs), T cells, and NK cells[2,3]. Despite its use for over 40 years, up to 40% of patients experience local recurrence, and up to 13% progress to muscle-invasive disease[4,5]. Radical cystectomy remains the only curative option for BCG-unresponsive patients, but is associated with significant morbidity, including urinary diversion and reduced quality of life[6,7].

Adaptive immune resistance is a central mechanism by which tumors evade otherwise effective immune surveillance[8]. The mechanisms underlying BCG resistance remain poorly understood. The six-week induction regimen was based on anecdotal data from the 1970s, and only one formal immunologic dosing study has been conducted, which did not address the duration or sustainability of the immune response[9,10]. While PD-L1 upregulation is observed in a subset of BCG-unresponsive tumors[11], PD-1/PD-L1 blockade shows limited efficacy in NMIBC, with durable response rates of ~19%, and PD-L1 levels fail to consistently predict treatment outcomes[5,11-14]. These data suggest additional resistance pathways are active in the bladder tumor microenvironment (TME).

HLA-E, a non-classical MHC class I molecule, delivers inhibitory signals via the NKG2A receptor expressed on NK cells and a subset of CD8 T cells[15-19]. Preclinical studies have demonstrated that blockade of NKG2A enhances cytotoxic activity of both NK and CD8 T cells, even in PD-1-resistant models[15,18]. Clinically, dual checkpoint blockade with anti-NKG2A (monalizumab) and anti-PD-L1 (durvalumab) doubled progression-free survival in patients with unresectable NSCLC compared to PD-L1 monotherapy[20,21]. We previously showed the importance of the HLA-E/NKG2A axis in modulating the functions of NK-like CD8 T cells in bladder cancer, with a heavy focus on treatment-naïve and muscle-invasive tumors[17].

In this study, we demonstrate that BCG therapy stimulates IFN-γ production by immune cells within bladder tissue, which in turn not only upregulates PD-L1 on tumor and immune cells but also upregulates HLA-E expression on bladder tumor cells. These HLA-E-expressing tumor cells co-localize with NKG2A NK and T cells, whose infiltration is enhanced by BCG-induced chemoattractants. NKG2A NK and T cells from BCG-treated tumors exhibit impaired TCR-independent, NK-like helper and cytotoxic functions due to inhibitory interactions with HLA-E and PD-L1. Blocking NKG2A and PD-L1 restores their effector functions, supporting the potential of this combination therapy to overcome resistance in BCG-unresponsive non–muscle-invasive bladder cancer.

RESULTS

HLA-E increases on tumor cells upon BCG treatment and associates with proximity with NKG2A$^+$ NK cells and T cells

We previously demonstrated that HLA-E expression in bladder tumors decreases as the disease progresses, although expression levels were highly variable at the non-muscle invasive (NMI) stage[17]. We here investigated the effects of BCG therapy on HLA-E expression within the NMI bladder tumor micro-environment. We first profiled HLA-E expression by multiplexed immunohistochemistry (IHC) on 41 bladder tumor sections (840,348 cells in total) from BCG-naïve (n=17) and BCG-treated (n=24) patients. We identified tumor cells and adjacent non-tumor epithelial cells as positive and negative for pan-cytokeratin, respectively (Figure 1A and 1B). HLA-E^{bright} tumor cells were significantly more abundant in BCG-treated unresponsive tumors (mean frequency 43.6%) compared to BCG-naïve tumors (mean frequency of tumor cells: 43.6% vs 10.3%, p=0.0002) (Figure 1C). Further, within BCG-treated tumors, we observed significantly higher HLA-E expression on tumor cells compared to normal epithelium in adjacent, non-involved tissue (mean frequency of HLA-E^{bright} epithelial cells 21.6% vs 71.2%, p<0.0001) (Figure 1D).

We next profiled abundance of NKG2A expression on CD3$^+$ (T cells) and CD3$^-$ (NK cells) cells in bladder tumors as well as their proximity to HLA-E^{bright} vs HLA-E$^{dim/neg}$ tumor cells (Figure 1E). We observed a significant enrichment of NKG2A-expressing cells in BCG-unresponsive tumors (Figure 1F). NKG2A$^+$ cells were comprised of similar proportions of NK and T cells in BCG-naïve and -unresponsive tumors (Figure 1G). Proximity analyses revealed that NKG2A NK and T cells were preferentially localized near HLA-E^{bright} tumor cells, rather than HLA-E^{dim} tumor cells (NKG2A$^+$ NK: p=1.7e-13, NKG2A$^+$ T cells: p=1e-15). Finally, we performed proximity ligation analysis of HLA-E and NKG2A

interactions on bladder tumor sections from BCG-naïve (n=6) and BCG-unresponsive (n=4) patients (Figure 1I). HLA-E and NKG2A interactions were increased in BCG-unresponsive tumors (p=0.009) (Figure 1J). Overall, our results indicate a higher prevalence of an engaged HLA-E/NKG2A axis in bladder tissue following recurrence in BCG-treated NMI bladder cancer patients.

BCG therapy induces IFN-□ secretion, that can drive HLA-E expression levels on tumor cells

We next performed targeted RNA sequencing using multiplexed in situ hybridization on BCG-naive (n=17) and BCG-unresponsive (n=19) tumors (Table S1). BCG-unresponsive tumors at the time of recurrence were significantly enriched in gene pathways associated with numerous proinflammatory pathways, including IFN-γ response signature, tumor inflammation and modulation of T cell function (Figure S1A). *HLA-E* and *NKG2A* were represented in the lymphocyte trafficking and the cytotoxic lymphocytes pathways, respectively.

The strong IFN-γ signature and enrichment of HLA-E^{bright} tumor cells in BCG-unresponsive tumors led us to examine whether IFN-γ contributes to HLA-E upregulation on tumor cells in the recurrent TME after BCG exposure. We first performed proteomic analyses (Olink) in urine supernatants of bladder cancer patients undergoing BCG therapy. Prior to BCG treatment ("Dose 1"), IFN-γ concentration in urine was comparable in BCG-responsive and BCG-unresponsive patients (Figure S1B). IFN-γ levels then increased significantly during the six-dose induction cycle of BCG treatment. Following BCG treatment, IFN-γ concentration in urine was higher in patients experiencing recurrence, compared to patients with no evidence of disease (Figure 2A). To assess IFN-γ-driven tumor-intrinsic effects, primary NMIBC tumor cells (n=10) and historical bladder cancer lines were cultured with recombinant IFN-γ. Wild-type ("WT") K562 cells, lacking class I HLA, remained unresponsive, while HLA-E-transduced K562 cells served as positive controls. Across all primary tumor and bladder cancer line samples, IFN-γ significantly upregulated PD-L1 and HLA-E expression, implicating this cytokine in promoting adaptive resistance (Figure 2B). We then profiled by single-cell RNA sequencing (scRNAseq) the expression of *IFNG* in non-muscle invasive bladder tumors (n=7). Using graph-based clustering, we identified twenty-two cell populations, including immune cells, nonhematopoietic stromal cells, normal epithelial cells and tumor cells (Figure 2C, Table S2). Of all the *IFNG*^{high} cells analyzed, *IFNG* was the most highly expressed in CD8 T cells, CD4 T cells, NK cells and proliferating T cells, with additional intermediate expression in myeloid cells (macrophages, monocytes, dendritic cells) (Figure 2D, Figure S1C). Collectively, our

findings suggest that IFN-γ is produced upon BCG treatment and contributes to the elevated tumor HLA-E expression in patients with high-grade BCG-unresponsive disease.

HLA-E^{high} tumors are in proximity with cytolytic cells in the bladder tumor microenvironment

To spatially resolve the relationships between *HLA-E*^{high} tumor cells, stroma and immune infiltrates, we performed 10x Visium^{TM} spatial transcriptomics (ST-seq) analysis of frozen bladder tumor sections from treatment-naïve (n=4; 5767 Visium spots) and BCG-unresponsive (n=4; 7182 Visium spots) tumors (Table S1). Clustering analysis based on the gene content and the regional features of the tumor tissue revealed 12 unique clusters, where the least represented cluster (cluster 12) remained unclassified and was removed from subsequent analyses (Figure 3A). Clusters were annotated based on their proportional composition of immune, stromal and/or tumor cells defined using gene signatures derived from scRNAseq analysis (Figure 3B). NK and CD8 T cells were mostly represented in five clusters (0, 1, 4, 7, 9), alongside other immune subpopulations, as well as stromal and tumor cells. We profiled the relative abundance of each spatial cluster between BCG-naïve and BCG-unresponsive tumors (Figure 3C) and observed substantial differences, where NK/T cell-containing spatial clusters 0, 4 and 6 were strongly enriched in BCG-unresponsive tumors, while the neutrophil/myeloid cell/tumor cell-containing cluster 2 was enriched in BCG-naïve tumors (Figure 3C-3E, S2A). We then performed neighborhood analyses to measure the proximity of *HLA-E*^{high} and *HLA-E*^{low} tumor cells to CD8 T cells, regulatory T cells (Tregs), and NK cells. ST-seq Visium^{TM} spots are 55µm, so deconvolution analyses were initially performed to better define which cell lineages are represented in each spot, as well as their relative abundances. In BCG-unresponsive tumors, NK cells, CD8 T cells and Tregs were significantly closer to *HLA-E*^{HIGH} tumor cells compared to *HLA-E*^{LOW} tumor cells, while no differences were observed in BCG-naïve tumors (Figure 3F-3G, S2B). Collectively, our findings demonstrate that HLA-E-expressing bladder tumors are in close proximity with cytolytic immune cells in the bladder tumor microenvironment upon BCG treatment.

Geographic organization and cellular interactions in the tumor segregate the microenvironment through local chemotactic hubs while fueling tumor growth

To better understand why *HLA-E* expression on tumor cells stratifies their proximity to immune effector cells, we profiled bladder tumor cell composition by scRNAseq in treatment-naive NMI bladder tumors (n=3) and in bladder tumors (n=4) from patients who recurred after BCG therapy (Table S1). UMAP clustering analysis revealed seven major subsets of tumor cells (Figure 4A, Table S2) with varying *HLA-*

E expression and distribution depending on BCG exposure (Figure 4B). Cluster B7 displayed the highest expression of *HLA-E* and was the most represented in BCG-unresponsive patients. The transcriptomic signature of bladder tumors expressing high *HLA-E* levels was enriched in genes associated with inflammation and response to interferons (IFN-α, IFN-□), compared to their *HLA-E*^{low} counterparts (Figure 4C). *HLA-E*^{low} tumor cells were significantly more proliferative (*MKI67*) compared to *HLA-E*^{high} tumor cells (p= 2.1e-179). Conversely, *HLA-E*^{high} tumor cells displayed significantly greater expression of *ACKR3* (CXCR7) (p= 3.5e-57) and to a lesser extent *CXCR4* (p= 1.7e-50) (Figure 4D). The ligands for CXCR4 and CXCR7 include CXCL11 and CXCL12, which gene expressions in the bladder TME were the highest in myeloid cells and stromal cells, respectively (Figure S3A). To better understand how these chemotactic networks affect the spatial organization of tumor cells within the TME, we applied the scRNAseq gene signatures to ST-sequencing. *CXCL11* gene did not pass the quality control test for spatial transcriptomics. We therefore evaluated the proximity of the *HLA-E*$^{high/low}$ tumor cells to *CXCL12*$^{high/low}$ stromal cells. We found *HLA-E*^{high} and *HLA-E*^{low} bladder tumors to be spatially distinct, with *HLA-E*^{high} tumors being closer to areas displaying higher stromal expression of their chemokine receptor ligand, *CXCL12,* while no difference was observed when comparing their proximity to *CXCL12*^{low} stromal cells (Figure 4E-F, Figure S3B-C).

We next examined the spatial relationships between NK and CD8 T cells and their surrounding immunosuppressive networks. In our scRNAseq data, *HLA-E* was most highly expressed in neutrophils. Neutrophils also displayed elevated expression of genes encoding additional activating ligands for T cells and NK cells, including the CD7 ligand (*SECTM1*), the LFA-1 ligand (*ICAM3)* and the ligand for the T cell immune checkpoint BTLA (*TNFRSF14)* (Table S2, Figure 4G). These findings suggest potential interactions between neutrophils and NK/CD8 T cells. Using ST-sequencing, we further demonstrated that neutrophils are positioned in closer proximity to NK and CD8 T cells within the bladder TME (Figure 4H-I, S3D). mReg DCs were recently described as mature DCs that express high levels of immunoregulatory molecules. Accordingly, mReg DCs expressed the highest levels of the gene encoding for PD-L1 (*CD274)* together with high expression of *CMTM6*, a stabilizer of PD-L1 at the cell surface[22,23] (Table S2). mReg DCs also showed high expression of ligands for the TIGIT (*NECTIN-2*), CTLA-4 *(CD80, CD86*), CD200R (*CD200*) and Tim-3 *(LGALS9*) immune checkpoint pathways (Table S2, Figure 4J). mReg DCs were additionally located in close proximity to NK and CD8 T cells in the bladder TME (Figure 4K-L, Figure S3E). Collectively, these results highlight a spatial tumor dichotomy and show that

NK and CD8 T cells are associated with neutrophil- and mReg DCs-driven immunosuppressive networks within the bladder TME.

KLRC1^{high} NK and CD8 T cells offer specialized helper and cytolytic effector functions in bladder tumors.

We next characterized the NKG2A^{+} cell compartment in NMI tumors in response to BCG treatment. We first profiled NK cell transcriptomic signatures by single-cell RNA sequencing. Building on two recent seminal resources for transcriptional reference mapping of human NK cells in solid tissues[24,25], we integrated the newly defined gene signatures to annotate functional states to bladder tumor-derived NK cells: Group 1 stressed CD56^{bright}, Group 2 typical CD56^{bright}, Group 3 effector CD56^{dim}, Group 4 adaptive CD56^{dim}, Group 5 activated CD56^{dim} and Group 6 typical CD56^{dim} NK cells (Figure 5A, Table S3). Those groups mirrored the five NK subgroups that we obtained by unbiased clustering, with Groups 1 and 2 NK cells representing approximately 80% of the total tumor-infiltrating NK cells (Figure S4A, Table S3). We similarly referenced mapped gene signatures for NK1, NK2, and NK3 subsets as recently demonstrated by Rebuffet et al[25,26], where these definitions most closely reflect a traditional developmental trajectory of NK cells across human tissues. NK2 and NK-intermediate cells represent immature CD56^{bright} NK cells, while NK3 cells include terminally mature and adaptive NK cells. Our comparative analysis revealed an enrichment of NK-intermediate cells representing the original clusters 1 and 2, and NK1B cells representing the original clusters 3 and 4. Both NK1B and NK-intermediate signatures were shared among the original cluster 5 suggesting transitional properties of this NK cell subset (Figure S4A and S4B, Table S3). Group 2 NK cells were the most abundant NK cell subset in the bladder TME, independently of BCG treatment status (Figure 5B), and expressed the highest levels of *KLRC1* (Figure 5C). They tracked very closely with previous descriptions of this functional state across many other human tissues by Netskar et al[24]. We then evaluated the transcriptome of NK cells depending on their expression of *KLRC1*. *KLRC1*^{high} cells displayed stronger expression of genes encoding tissue-resident memory markers (*ZNF683*, *ITGAE*, *CXCR6*), pro-inflammatory chemokines (*XCL2, CSF1*) and NK checkpoints (*TNFRSF18*, *CD96*, *TIGIT*) while *KLRC1*^{low} cells displayed a stronger cytolytic and activating signatures *(GZMB, GZMH, GZMM, NKG7, FGFBP2, IFNG, CD69)* (Figure 5D, Table S3).

We recently showed that the effects of NKG2A extend beyond NK cells in bladder cancer, where its expression is associated with T cell exhaustion and the acquisition of NK-like functions by CD8 T cells[17]. We therefore investigated the expression of NKG2A on CD8 T cells in NMI tumors. Unbiased clustering

analysis revealed eight main CD8 T cell clusters, with a trend toward enrichment of the "*NFIL3* effector", "Early exhausted" and "Terminally exhausted" clusters following BCG treatment (Figure 5E-F, Table S3). Those three clusters displayed the highest *KLRC1* expression (Figure 5G). We then profiled the transcriptome of CD8 T cells depending on *KLRC1* expression. *KLRC1*^{high} CD8 T cells showed higher expression of genes encoding T cell checkpoints (*TIGIT, ENTPD1, CTLA4*), tissue-residency memory molecules (*ITGA1*), NK cell activation markers (*CD226*), cytotoxic mediators *(FASLG, GNLY, GZMB*) and proliferation marker (*MKI67*) (Figure 5H, Table S3).

We next compared the transcriptome of *KLRC1*^{high} NK cells (Group 2 NK cells) and *KLRC1*^{high} CD8 T cells. In the bladder TME, Group 2 NK cell signature was more associated with the production of pro-inflammatory chemokines (*XCL1, XCL2)* and cytokines *(CSF1, AREG)*, while *KLRC1*^{high} CD8 T cells displayed higher levels of cytolytic mediators (*GZMA, FASLG*). The tissue-residency memory program was more pronounced in *KLRC1*^{high} NK cells but remained lower compared to *KLRC1*^{high} CD8 T cells. Another crucial distinction between those two subsets laid in the exclusive expression of T cell exhaustion markers by *KLRC1*^{high} CD8 T cells, Finally, while *CXCR3* was expressed in both *KLRC1*^{high} and *KLRC1*^{low} CD8 T cells, its expression levels were increased upon higher *KLRC1* expression in NK cells (Figure 5I, Table S3). CXCR3 is a chemokine receptor that promotes cell migration towards concentration gradients of CXCL9, CXCL10 and CXCL11. We found the genes encoding for these three chemokine ligands to be the most highly expressed in dendritic cells, macrophages and monocytes within the bladder TME (Figure S4C). To better understand the dynamic nature of this chemotactic signaling during BCG treatment, we sampled urine supernatants from patients with high-grade NMIBC before and during the six-week induction cycle and time of first cystoscopy (12-16 weeks) from two cohorts: Mount Sinai Hospital, New York, USA and Aarhus University, Aarhus, Denmark. We performed multiplexed qPCR by Olink Proteomics^{TM} to profile 92 soluble analytes associated with inflammation and immune response. In the Mount Sinai cohort, CXCL9, CXCL10, and CXCL11 were among the molecules that were upregulated upon the six BCG doses. Opportunistically, we had access to another clinical dataset of BCG-treated patients with NMIBC at Aarhus University with an overlapping but nonredundant Olink Proteomics^{TM} analysis. CXCL9, CXCL10, and CXCL11 were also upregulated following BCG exposure, at time of first cystoscopy (Figure S3D). Overall, our results suggest that the CXCR3 chemotactic axis might promote NKG2A^{+} NK and CD8 T cell migration within the bladder TME, where NKG2A expression on NK cells is linked to a pro-inflammatory helper profile, and its expression on CD8 T cells is linked to a cytolytic profile.

Cytolytic effector functions are impaired in BCG-treated tumors but can be effectively restored by anti-NKG2A and anti-PD-L1 blockade

In order to evaluate the potential for anti-NKG2A and anti-PD-L1 in restoring cytolytic functions upon BCG resistance, we tested the effects of the HLA-E/NKG2A and PD-1/PD-L1 axes on NK cells and NK-like CD8 T cell functions in BCG-treated bladder tumors. TILs were isolated from BCG-unresponsive tumors (n=4) and expanded up to 13 days in the presence of low dose IL-2, IL-7 and IL-15 as well as anti-CD3, -CD28 and -CD2 stimulating agents. TGF-β was added in the last three days to promote NKG2A expression, as we previously reported[17]. NK cells and CD8 T cells made up 0.7% and 16% of all expanded TILs and NKG2A was expressed in 29% and 13% of NK and CD8 T cells, respectively (Figure S5A-S5B). We measured TCR-independent NK-like functions of NK cells and CD8 T cells by co-culturing expanded TILs with an artificial HLA class $I^{-/-}$ K562 acute myeloid leukemia tumor model, as previously described[17]. K562 cells that were stably transduced with HLA-E were pre-stimulated during 24 hours with recombinant IFN-γ in order to induce PD-L1 expression (Figure S5C). Flow cytometry was performed upon 6h co-cultures of TILs with HLA-$E^{+/-}$ PD-$L1^{+/-}$ K562 cells in the presence or absence of anti-PD-L1 blockade or combined anti-PD-L1 and anti-NKG2A blockade (Figure 6A). CD56 was then used as a surrogate for NKG2A as use of monalizumab precluded our ability for detecting NKG2A with antibodies by flow cytometry. NK cells and $CD56^+$ CD8 T cells displayed greater degranulation and IFN-γ production to HLA class $I^{-/-}$ K562 cells compared to *ex vivo* activity, and their response was diminished when K562 cells stably expressed HLA-E or HLA-E and PD-L1. NK cell activation was restored in response to both HLA-E^+ and HLA-E^+ PD-$L1^+$ K562 cells when pre-treated with anti-NKG2A Ab alone or in combination with anti-PD-L1 Ab (CD107a: 2.1-fold increase, p=0.02; IFN-γ: 1.6-fold increase, p=0.05). TCR-independent activation of $CD56^+$ CD8 TILs tended to increase upon anti-NKG2A blockade, and this increase became significant in the presence of both anti-NKG2A and anti-PD-L1 Abs (CD107a: 1.75-fold increase, p=0.02; IFN-γ: 1.8-fold increase, p=0.007) (Figure 6B). Collectively, the data show impairment of NK cell and NK-like CD8 T cell functions through the HLA-E/NKG2A and PD-L1/PD-1 immunosuppressive axes and suggest a potential effect of anti-NKG2A and anti-PD-L1 blockade in managing tumor recurrence after failing BCG therapy.

DISCUSSION

Intravesical administration of BCG is initiated as adjuvant immunotherapy, as complete tumor resection is the initial diagnostic and therapeutic step in NMIBC. As a result, standard of care BCG immunotherapy is delivered into an inflamed bladder mucosa with minimal residual disease rather than against an established tumor[27]. Yet, treatment improvements for NMIBC, especially for BCG-unresponsive patients, remain limited. This may reflect the lack of work connecting the timing of tumor recurrence, the reasoning for the recurrence, and the state of the immune system at the time of recurrence. Poor dosing study designs and lack of understanding of the mechanisms underlying a therapeutic response to intravesical BCG have led to a significant gap in knowledge and benefit for patients with NMIBC compared to muscle-invasive or metastatic disease.

Adaptive resistance can be driven by tumor-intrinsic and/or extrinsic mechanisms in overcoming immune pressures[28-31]. This complex process involves multiple non-redundant checkpoints that have evolved in humans. Cancers highjack a critical function applied in normal tissues, whereby negative feedback "turns off" immune responses following resolution of, e.g., infection or wound. For instance, evidence from mouse and human studies demonstrates that interferons, while stimulating a robust anti-tumor response, also upregulate immune-suppressive factors in the setting of prolonged activation. In melanoma, IFN-γ from CD8 T cells was shown to upregulate tumor PD-L1 expression and mediate infiltration of $FOXP3^+$ regulatory T cell pathways within the TME[32]. In a broader meta-analysis across 18 tumor indications, including bladder cancer, inflammatory mediators including IFN-γ were associated with inhibitory immune checkpoints, including PD-L1/L2[33,34]. Despite emerging evidence positioning pro-tumorigenic roles for IFN-γ, there are well-established anti-tumor functions mediated through IFN-γ that are critical for anti-PD-L1 immunotherapy[35]. Anti-tumor inflammation, therefore, exists along a continuum where an equilibrium is necessary for appropriate immunotherapeutic efficacy[36].

In our investigation, we examined the primary resistance mechanisms to BCG therapy and assessed the impact of BCG-induced inflammation on the dynamic interplay between tumor and immune cell populations. Using both prospective and retrospective NMIBC specimens collected before, during, and after BCG treatment, we observed a pervasive inflammatory response in both BCG responders and non-responders. Our analyses revealed significantly higher expression of HLA-E in bladder tumors which recurred after BCG therapy compared to their BCG-naïve counterparts. This upregulation of HLA-E may be driven by the sustained and elevated IFN-γ concentrations observed at time of recurrence. Tumors with the highest HLA-E expression were found in closest proximity to NKG2A□ NK and T cells,

underscoring the potential importance of the HLA-E/NKG2A immune checkpoint axis in BCG resistance. A novel aspect of our study is the spatially resolved insight into the consequences of IFN-γ dysregulation and patterns of tumor-immune cell homing. Spatial and scRNAseq analyses of the bladder TME demonstrated that NK cells and NKG2A^{+} CD8 T cells move closer to HLA-E^{high} tumor cells in recurrent tumor settings, which is mediated through a network of chemotactic signaling. Immunosuppressive pathways associated with neutrophils and mReg DCs were also found in close proximity to NK cells and CD8 T cells. BCG treatment induced expression of ligands for CXCR3, that is expressed on NKG2A^{+} NK cells and CD8 T cells, suggesting the involvement of this chemotactic pathway in the recruitment of those effectors in the bladder TME. Tumor cells were spatially distinct based on their expression of HLA-E, with *HLA-E*^{high} tumor cells being specifically close to stromal cells that express CXCL12. This suggests an immune evasion mechanism in which HLA-E^{high} tumor cells - responding to stroma-derived CXCL12 - may act as 'decoys' to help protect HLA class I–negative tumor cells.

We also identified NKG2A receptor expression as a key factor in shaping the anti-tumor effector functions of NK and CD8 T cells in the bladder TME. NKG2A NK cells displayed a stronger helper profile, whereas NKG2A CD8 T cells exhibited a more potent cytolytic profile. This suggests that NKG2A expression on NK and CD8 T cells encodes distinct yet complementary programs that may cooperate in eliminating tumor cells lacking HLA-E. NKG2A-enriched NK and CD8 T cells from BCG-unresponsive patients responded to *in vitro* stimulation with MHCI-lacking K562 tumor cells, in line with our previous findings showing that NKG2A^{+} CD8 T cells display TCR-independent innate-like functions[17]. However, their functional response to HLA-E PD-L1 K562 tumor cells was robustly increased in the presence of combined NKG2A/PD-L1 blockade. Collectively, our findings depict a landscape of immune dysregulation in BCG-resistant bladder cancer, prominently characterized by elevated tumor HLA-E expression, altered immune–tumor spatial relationships, and chemokine-driven cell positioning, with implications for targeting the HLA-E/NKG2A axis in therapy.

Our findings suggest that all NMIBC patients at the time of tumor recurrence show signs of a hallmark anti-tumor immune response dominantly driven by IFN-γ. BCG-unresponsive tumors see uniform increases in chemotactic cytokines and inflammatory pathways that should otherwise function to suppress tumor growth. Further, increased expression of inhibitory ligands on BCG-unresponsive tumor cells was observed, suggesting that inflammatory stimuli had been prolonged and triggered feedback mechanisms responsible for immune evasion. These results are seen on multiple levels, including bulk

and single-cell RNA sequencing, spatial sequencing, multiplex imaging, and flow cytometry. This implies that when tumors recur, for reasons beyond the scope of this study, they are met by an overactive status of the immune system ill-equipped to combat them. Here, we, for the first time, link both established and novel concepts to identify a key mechanism of resistance to immunotherapy in bladder cancer. This might not be unique to bladder cancer, but BCG as a treatment for bladder cancer uniquely exacerbates this phenomenon.

Previous analyses profiling urine analytes between the BCG naïve and third dose timepoints demonstrated that three doses of BCG induced an inflammatory response hundreds of times above baseline levels of cytokines, including but not limited to IP-10, MIP-1β, IL-8, IL-6, and TNFα[37]. Importantly, the third dose-response dwarfed the magnitude of the first dose-response, suggesting that repeated exposure increases the magnitude of inflammation[37]. While these data did not profile out to the time of tumor recurrence, they lend credence to the theory that all patients experience a ubiquitous and increasingly powerful immune response to repeated doses of BCG. Importantly, our findings confirm these previous observations. Further, they demonstrate that inflammation is sustained even throughout the six-week treatment interruption at time of first cystoscopy and do not equilibrate to baseline levels.

Clinical efficacy in checkpoint blockade is dependent on reinvigorating effector cells expressing high levels of the targeted checkpoint(s). Our findings reinforce both the use of NKG2A to reinvigorate cytolytic effector and helper functions by NK and CD8 T cells, as well as the potential to exploit a critical mechanism of tumor resistance, whereby chemokines lure in effector cells to take on exhausted phenotypes. Recent clinical evidence emerging from interim results of the randomly controlled Phase II COAST trial demonstrated significantly prolonged survival in non-small cell lung cancer (NSCLC) patients treated with monalizumab combined with durvalumab compared to standard of care durvalumab alone for treatment of unresectable stage 3 NSCLC[20]. This combination is currently being further evaluated in a larger Phase III trial (PACIFIC-9, NCT05221840) following these promising early results. Collectively, our data demonstrate that elevated tumor expression of HLA-E and PD-L1 and chronic activation of NKG2A-expressing NK and CD8 T cells are hallmark features of resistance to BCG immunotherapy in NMI bladder tumors and that integrating NKG2A-blockade into combination immunotherapy strategies may prove particularly effective in settings of BCG-unresponsive, high-grade NMIBC.

Based on the data generated from this study, we recently designed and began accrual of a Phase 2 trial of durvalumab (MEDI4736) and monalizumab in NMIBC. The Phase 2 trial: ENHANCE (**E**levated **N**KG2A and **H**LA-E **A**mplify **N**K and **C**D8 T-cell **E**ngagers) (clinicaltrials.gov ID: NCT06503614) investigates the effects of monalizumab (anti-NKG2A Ab) plus durvalumab (anti-PD-L1 Ab) for combination checkpoint blockade in high-grade BCG-unresponsive (and exposed) NMIBC as a bladder-sparing immunotherapy strategy. In this trial, an exploratory objective is to assess the relationship between baseline tumor HLA-E expression and NKG2A abundance and clinical outcomes to facilitate development of HLA-E as a potential biomarker for patient selection in future clinical trials intending to target NKG2A.

Our study has notable limitations. Our sample sizes, while being the largest NMIBC spatial sequencing and single-cell RNA sequencing cohorts available, are small and present a potentially limited view of the disease. Further, certain genes of relevance, e.g., *KLRC1, CXCL9, CXCL10, CXCL11, CXCR3, CXCR4* did not pass our quality control and, therefore, had to be omitted for subsequent spatial sequencing analyses. Additionally, as BCG is administered as an adjuvant therapy, we are only afforded access to bladder tissues after treatment if tumor recurs. Thus, it was not feasible to profile bladder tissues in the absence of tumor following exposure to BCG. Future studies might benefit from a neoadjuvant approach, where tumor tissue can be sampled and profiled for potential therapeutic responses to BCG.

Collectively, our analyses suggest that the current guidelines on immunotherapy for BCG-unresponsive NMIBC could be improved via a multi-cell-targeting immunotherapy approach that exploits NK cells to improve T cell-targeted immunotherapies. Randomized trials from bladder and other tumor indications have shown that PD-1/PD-L1 stratification fails to predict response to immunotherapy with anti-PD-1/PD-L1 antibodies: IMvigor210, JAVELIN bladder 100, and CheckMate-275 (NCT02108652, NCT01772004, NCT02387996) all saw that PD-1/PD-L1 biomarker stratification alone did not effectively stratify response rates. In comparison, recent results using *KLRC1* (NKG2A) expression in the pre-treatment tumor significantly improved predicted anti-PD-L1 response rates in the IMvigor210 cohort, but only in the $CD8^{high}$ *PDCD1* $(PD\text{-}1)^{high}$ group [17]. In fact, where IHC stratification of PD-L1 expression has failed to predict immunotherapeutic responses, *KLRC1* stratification in IMvigor210 showed protective effects were restricted to the PD-L1 IC high group. In conclusion, while our analysis does not exclude the presence of alternative checkpoints, it lends evidence to the hypothesis that combination immunotherapy strategies dually targeting NK and T cells may hold the key to improved outcomes for patients with high-grade NMIBC.

ACKNOWLEDGMENTS

We thank Mary Anne O'Donnell (Precision Immunology Institute, Icahn School of Medicine at Mount Sinai) for critically reviewing the manuscript; Deepta Bhattacharya (University of Arizona) for kindly providing HLA-E^{+} K562 tumors. We acknowledge the expertise and assistance of the Dean's Flow Cytometry Center of Research Excellence at Mount Sinai. The A.H. and J.P.S labs were supported by funding from P30CA196521, R01CA269954-01, R21CA274148, BCAN (Bladder Cancer Advocacy Network) No. 961726, R01CA301050, and R21AI130760A. The N.B. lab was supported by funding from the Department of Defense Peer Review Cancer Research program Translational team Award No. W81XWH1910269 and from the Parker Institute for Cancer Immunotherapy No.AGR-11611SOW1. The J.J.B-C lab was supported by funding from R01CA244780, R61CA278402, the Irma T. Hirschl Trust and the Emerging Leader Award from the Mark Foundation. The L.D lab was supported by funding from the Danish Cancer Society. The O.E lab was supported by the following grants: NCI250233, OT2CA297580, U24CA264032, R01AI187598, R01CA271915, U01DA058527, R01CA271619, R01CA271545, R01NS111997, R01NS127984, R01CA269954, U19AI168632, OT2OD032720, 80NSSC23K0832, CGCATF2023100030, HHWF240412, and LLS702723. A.N.M.R.S was part of the A.H lab as part of an existing collaboration with Dr. Leonardo Oliveira Reis (UroScience, University of Campinas-UNICAMP, Campinas, São Paulo, Brazil) and National Council for Scientific and Technological Development (CNPq-Brazil Edital 26/2021- Process 402562/2022-4) and received the following fellowship: CNPq-PDE process 201230/2024-0.

AUTHOR CONTRIBUTIONS

D.R., H.Y., Y.A.W., C.B., J.D., B.S., M.G., N.B., J.P.S., and A.H. conceived the project and experiments, analyzed the data and wrote the manuscript. J.P.S., R.M., P.W., M.G., and R.B. provided access to the human samples. Additionally, L.D. provided analyses on data derived from human samples at Aarhus University Hospital. D.R., H.Y., Y.A.W., C.B., A.D., S.B., W-M.S., J.D., B.S., D-F.R., F.P. E.M., A.T., J-A.C-F., B.D.H., T.S., S.V.L., S.H., J.K., performed the experiments or analyzed data. A.M.F, M.T., J.Z., K.G.B, L.W, R.P.S, S.S, Y-C.W, and Y.A.W. collected the RNA sequencing data. D.G., G.K., R.M.d-R, B.L., S.K-S. acquired sample data using Olink proteomics. T.H.T, M.G-B, R.B., E.H-S, E.M.M, C.B., R.F-G, M.S, H.R, A.N., G.D., and J.J.B-C. performed the imaging experiments. S.S., E.C-

T., D.P., and S.H. provided intellectual input. Authors affiliated with the Tisch Cancer Institute were supported by the National Cancer Institute Cancer Center Support Grant P30CA196521.

DECLARATION OF INTERESTS

A.H. receives research funds from Astra Zeneca and has recently served on the advisory boards of Immunorizon, Purple Biotech, enGene, and Moexa Pharmaceuticals. N.B. is an extramural member of the Parker Institute for Cancer Immunotherapy, receives research funds from Regeneron, Harbor Biomedical, DC Prime, and Dragonfly Therapeutics and is on the advisory boards of Neon Therapeutics, Novartis, Avidea, Boehringer Ingelheim, Rome Therapeutics, Rubius Therapeutics, Roswell Park Comprehensive Cancer Center, BreakBio, Carisma Therapeutics, CureVac, Genotwin, BioNTech, Gilead Therapeutics, Tempest Therapeutics, and the Cancer Research Institute. LD has sponsored research agreements with C2i Genomics, Veracyte, Natera, AstraZeneca, Photocure, and Ferring and serves in an advisory/consulting role for Ferring, MSD, Cystotech, and UroGen. LD has received speaker honoraria from AstraZeneca, Pfizer, and Roche.

MAIN FIGURE TITLES AND LEGENDS

Figure 1: HLA-E increases on tumor cells upon BCG treatment and associates with proximity with NKG2A$^+$ NK cells and T cells

(A-D) IHC was performed on bladder tumor and adjacent non-involved tissues from BCG-naïve and BCG-unresponsive NMIBC patients.

(A) Representative digital pathology analyses identifying tumor, adjacent tissue along with exposed areas of glass to be excluded from subsequent analyses.

(B) Representative density map showing gradient of HLA-E tumor expression.

(C) Summary analysis of frequency of tumor cells that are HLA-E-bright and HLA-E-dim/negative in BCG-naïve (n=17) and BCG-unresponsive ("unresp.", n=24) NMIBC tumors. The p-value was obtained using an independent two-sided t-test.

(D) Summary analysis of frequency of HLA-E^{bright} epithelial cells in tumor and adjacent, non-involved bladder tissues from BCG-unresponsive patients with NMIBC. The p-value was obtained using a paired t-test. Lines show matching samples from a same donor.

(E-J) IHC was performed on NMIBC tumors (n=41 tumors).

(E) Representative digital pathology analysis on one BCG-naïve and one BCG-unresponsive NMIBC tumor section highlighting nuclear expression of DAPI and identification of CD3$^+$NKG2A$^+$ T cells, CD3-NKG2A$^+$ NK cells and tumor cells with bright or dim/negative expression of HLA-E.

(F) Frequencies of NKG2A$^+$ cells in BCG-naïve (n=17) and BCG-unresponsive ("unresp.", n=24) tumors.

(G) Frequencies of NK cells within the NKG2A$^+$ cell compartment in BCG-naïve (n=17) and BCG-unresponsive (n=24) tumors.

(H) Proximity analysis measuring the cell distance from CD3$^-$ NKG2A$^+$ NK cells or CD3$^+$NKG2A$^+$ T cells and tumor cells, depending on the tumor cell expression of HLA-E. P-values were assessed via independent two-sided t-test.

(I-J) Interactions between HLA-E and NKG2A were profiled using an immunofluorescence-based proximity ligation assay in bladder tumors from NMIBC patients (n=10).

(I) Representative staining in one BCG-naïve (left) and one BCG-unresponsive (right) patient.

(J) Summary analysis of the interactions between HLA-E and NKG2A in BCG-naïve (n=6) and BCG-unresponsive (n=4) tumors. The p-value was assessed via independent two-sided t-test.

Figure 2: BCG therapy induces IFN-□ secretion, that increases HLA-E and PD-L1 expression levels on tumor cells

(A) Olink protein analysis was performed on urine supernatants of patients undergoing BCG therapy. IFN-□ concentrations were compared between dose 1 and dose 6 of the first induction cycle (left panel) and between non-evidence of disease (absence of tumor) and recurrence cases of BCG-treated patients (right panel). Lines show matching samples from a same patient. P-values were obtained with paired (left) or unpaired (right) t-tests.

(B) Flow cytometry was performed on primary $CD45^-$ tumor cells from NMIBC patients and immortalized bladder tumor lines *ex vivo* and upon 24 hour stimulation with rhIFN-□. Representative (left) and summary (right) expression of PD-L1 and HLA-E in triplicate experiments.

(C-D) Since-cell RNA sequencing was performed on *ex vivo* bladder tumors (n=3 BCG-naïve, n=4 BCG-unresponsive).

(C) UMAP clustering analysis. Each color represents a cluster.

(D) Distribution of the $IFNG^{high}$ cells across all clusters.

Figure 3: $HLA\text{-}E^{high}$ tumors are in proximity with cytolytic effector cells in the bladder tumor micro-environment

(A-G) Spatial transcriptomics sequencing (ST-seq) analysis was performed on NMIBC tumors (n=8).

(A) UMAP visualization of the ST-clusters. Each color represents one cluster.

(B) Relative composition of the ST-clusters across immune, stromal and tumor cell subtypes (columns) as defined by scRNAseq analysis. The size of each bubble indicates its relative enrichment and the shading of the surrounding boxes represents the significance by FDR (corrected p-values).

(C) Relative enrichment of each ST-cluster in BCG-naïve (N=4) and BCG-unresponsive (N=4) tumors.

(D) Distribution of each cluster in BCG-naïve and BCG-unresponsive tumor specimens. Each color represents one cluster.

(E) Representative ST-seq images showing the distribution of ST-clusters in one BCG-naïve (left) and one BCG-unresponsive (right) NMIBC tumor specimens. Each color represents one cluster.

(F) Representative ST-seq images from one BCG-naïve (left) and one BCG-unresponsive (right) NMIBC tumor specimens showing proximity analyses of $HLA\text{-}E^{low}$ and $HLA\text{-}E^{high}$ tumor cells as well as NK cells, CD8 T cells, and Tregs alone or in combination. Each dot represents one cell type.

(G) Summary comparisons of proximity of $HLA\text{-}E^{low}$ and $HLA\text{-}E^{high}$ tumor cells to NK cells, CD8 T cells and Tregs. p-values were determined using two-sided Wilcoxon test.

Figure 4: Geographic organization and cellular interactions in the tumor segregate the microenvironment through local chemotactic hubs while fueling tumor growth

(A-D) Single-cell RNA sequencing was performed on ex vivo bladder tumors (n=3 BCG-naïve, n=4 BCG-unresponsive) and tumor cells selected for further analyses.

(A) UMAP visualization of bladder tumor cells from unsupervised clustering. Each color represents one cluster.

(B) Average expression of HLA-E per cluster (left) and distribution of the bladder tumor cell clusters in BCG-naïve and BCG-unresponsive NMIBC tumors (right).

(C) Pathway analysis of Hallmark gene networks that are significantly differentially expressed on HLA-E^{high} and HLA-E^{low} bladder tumor cells.

(D) Differential expression in HLA-E^{high} and HLA-E^{low} tumors of key genes of interest.

(E-L) Spatial transcriptomics sequencing (ST-seq) was performed on ex vivo bladder tumors (n=4 BCG-naïve, n=4 BCG-unresponsive)

(E) Representative ST-seq image from one NMIBC tumor highlighting the proximity of stromal cells and tumor cells according to *HLA-E* expression in the tumors and *CXCL12* expression in the stromal cells.

(F) Summary graph of the proximity between *HLA-*$E^{low/high}$ tumors and *CXCL12*^{high} spots.

(G) Average expression in all cell populations of genes of interest that are upregulated in neutrophils and their ligands/receptors.

(H) Representative ST-seq image from one NMIBC tumor highlighting the proximity of NK and CD8 T cells to neutrophils.

(I) Summary graph of the neutrophils deconvolution scores in spots that are neighbors of NK/CD8T cells vs other cells.

(J) Average expression in all cell populations of genes of interest that are upregulated in mReg DCs and their ligands/receptors.

(K) Representative ST-seq image from one NMIBC tumor highlighting the proximity of NK and CD8 T cells to mReg DCs.

(L) Summary graph of the mReg DCs deconvolution scores in spots that are neighbors of NK/CD8T cells vs other cells

Figure 5: Bladder tumors are enriched with *KLRC1*^{high} NK and CD8 T cells that offer helper and cytolytic effector functions.

(A-I) Single-cell RNA sequencing was performed on *ex vivo* bladder tumors (n=3 BCG-naïve, n=4 BCG-unresponsive). Further analyses were then performed on selected NK cells or CD8 T cells.

(A) UMAP visualization of NK cells from the bladder tumors, showing the Groups 1-6 clusters defined by Netskar et al[24]

(B) Distribution of the Groups 1-6 NK clusters in BCG-naïve and BCG-unresponsive tumors

(C) For each of the six NK clusters, violin plot displaying *KLRC1* expression (top) and list of key genes of interests (bottom)

(D) Differential transcriptomic signature between *KLRC1*^{high} and *KLRC1*^{low} NK cells.

(E) UMAP visualization of CD8 T cells from the bladder tumors, showing eight clusters from unbiased cluster analysis

(F) Distribution of the eight CD8 T cell clusters in BCG-naïve and BCG-unresponsive tumors

(G) For each of the eight CD8 T cell clusters, violin plot displaying *KLRC1* expression (top) and list of key genes of interests (bottom)

(H) Differential transcriptomic signature between *KLRC1*^{high} and *KLRC1*^{low} CD8 T cells.

(I) Heatmap displaying the expression of key genes of interest between Groups 1-6 NK cells and *KLRC1*$^{high/low}$ CD8 T cells.

Figure 6: NKG2A and PD-L1 blockade increase NK and CD8 T cell-mediated antitumor activity in BCG-unresponsive patients

(A-C) Tumor-infiltrating lymphocytes (TILs) were expanded *in vitro* from BCG-unresponsive bladder tumors (n=4) during 13 days in the presence of IL-2 and CD3/CD28/CD2 T cell activator, prior to a 6-hour co-culture with K562 cell lines. NK and CD8 T cell functions were then assessed using flow cytometry. “WT” K562: Wild-type (HLA-E^{-}) K562 ; “E+” K562: HLA-E-induced K562; “L1+E+” K562: HLA-E induced K562 that were stimulated with IFN-□ to induce PD-L1 expression.

(A) Representative and **(B)** summary expression of IFN-□ and CD107a by NK cells and CD56^{+} CD8 T cells after co-culture with HLA-E$^{-/+}$ PD-L1$^{-/+}$ K562 cell lines in the presence or absence of anti-PDL1 and/or anti-NKG2A antibodies.

STAR METHODS

RESOURCE AVAILABILITY

Lead contact

Further information and requests for resources and reagents should be directed to and will be fulfilled by the Lead Contact Amir Horowitz (amir.horowitz@mssm.edu).

Materials availability

This study did not generate new unique reagents.

Data and Code availability

The single-cell RNAsequencing and spatial-sequencing data generated by the authors have been uploaded to the Gene Expression Omnibus (GSE276014 and GSE276015) and will be made publicly available upon publication of this manuscript.

The algorithms used in this study will be made available at https://github.com.

KEY RESOURCE TABLE

REAGENT or RESOURCE	SOURCE	IDENTIFIER
Antibodies		
Anti-human HLA-E PerCPCy5.5	BioLegend	Cat#342609; RRID#AB_2565434
Anti-human PD-L1 PE	BioLegend	Cat#124308; RRID#AB_2073556
Anti-human CD3 (IHC)	Abcam	Cat#ab135372; RRID#AB_2884903
Anti-human NKp46 (IHC)	Innate Pharma	N/A
Anti-human HLA-E (IHC)	Abcam	Cat#ab2216; RRID#AB_302895
Anti-human NKG2A (IHC)	Abcam	Cat#ab260035; RRID#AB_2895228
Anti-human CD107a BV785	BioLegend	Cat#328644; RRID#AB_2565968
Anti-human IFNγ PE-Cy7	BioLegend	Cat#502527; RRID#AB_1626154
Durvalumab	AstraZeneca	N/A

Monalizumab	AstraZeneca	N/A
Chemicals, peptides and recombinant proteins		
RPMI-1640 Medium	Thermo Fischer Scientific	Cat#22400-089
DPBS, no calcium, no magnesium	Thermo Fischer Scientific	Cat#14190-250
Fetal Bovine Serum	Thermo Fischer Scientific	Cat#16000044
L-glutamine	Corning Inc.	Cat#25-005-CI
Human AB serum	Millipore Sigma	Cat#H4522
MEM Non essential amino acids	Thermo Fisher Scientific	Cat#11140050
Sodium Pyruvate	Thermo Fisher Scientific	Cat#11360070
Penicillin-Streptomycin	Thermo Fisher Scientific	Cat#15140122
Recombinant human IL-2	Clinigen, Inc.	Proleukin
Recombinant human IL-7	Peprotech	Cat#200-07
Recombinant human IL-12p70	Peprotech	Cat#200-12
Recombinant human IL-15	Peprotech	Cat#200-15
0.5M EDTA	Thermo Fischer Scientific	Cat#15575-020
DMSO	Fisher Scientific	Cat#D1391
Recombinant Human IFN-□		
Diluent 2 NT solution	Navinci	Cat#NF.1.100.03
Buffer 1 NT	Navinci	Cat#NB.2.100.17
Enzyme 1 NT	Navinci	Cat#NF.2.100.11
Buffer 2 NT	Navinci	Cat#NT.2.100.01
Enzyme 2 NT	Navinci	Cat#NF.2.100.15
Post-block NT reagent	Navinci	Cat#NF.1.100.01
Post-block supplement NT	Navinci	Cat#NT.2.100.04
Prolong Gold Antifade reagent	Invitrogen	Cat#P36930
DAPI	BioLegend	Cat#422801
Monensin	BioLegend	Cat#420701

Brefeldin A	BioLegend	Cat#420601
Paraformaldehyde	Electron Microscopy Sciences	Cat#15710
Anti-mouse Navenibody M1 NT	Navinci	Cat#NB.1.100.06
Anti-rabbit Navenibody R2 NT	Navinci	Cat#NB.1.100.07
Critical commercial assays		
Human tumor dissociation kit	Miltenyi Biotec	Cat#130-095-929
ImmunoCult™Human CD3/CD28/CD2 T Cell Activator	Stemcell Technologies	Cat#10970
ImmunoCult™Human CD3/CD28 T Cell Activator	Stemcell Technologies	Cat#10971
Zombie NIR™ Fixable Viability Kit	BioLegend	Cat#423106
Deposited data		
scRNAseq data	N/A	GSE276014
Spatial-seq data	N/A	GSE276015
Experimental models: Cell lines		
K562	Gift from D. Bhattacharya	N/A
HLA-E+ K562	Gift from D. Bhattacharya	N/A
253J	Provided by J. Sfakianos	RRID: CVCL_7935
639V	Provided by J. Sfakianos	RRID: CVCL_1048
5637	Provided by J. Sfakianos	RRID: CVCL_0126
J82	Provided by J. Sfakianos	RRID: CVCL_0359
KU-19-19	Provided by J. Sfakianos	RRID: CVCL_1344
MGHU3	Provided by J. Sfakianos	RRID: CVCL_9827
RT4	Provided by J. Sfakianos	RRID: CVCL_0036
RT112	Provided by J. Sfakianos	RRID: CVCL_1670
SW1710	Provided by J. Sfakianos	RRID: CVCL_1721

T24	Provided by J. Sfakianos	RRID: CVCL_0554
UMUC3	Provided by J. Sfakianos	RRID: CVCL_1783
Software and algorithms		
GraphPad Prism Software v10.5.0	GraphPad Software, Inc.	https://www.graphpad.com
Cytobank	Beckman Coulter	https://cytobank.org
Python 3.8.1	Python Software Foundation	https://www.python.org/
HALO™ Software	Indica Labs, Inc.	https://indicalab.com/halo/
LAS X software, v3.7.5.24914	Leica Microsystems	https://www.leica-microsystems.com/products/microscope-software/p/leica-las-x-ls/#
Imaris software 10.1.1	Oxford Instruments	https://imaris.oxinst.com/
Cytobank	Beckman Coulter	https://cytobank.org
R	R Foundation	https://www.r-project.org
Space Ranger Software Suite v.1.0	10x Genomics, Inc.	https://www.10xgenomics.com/software/space-ranger
Seurat v5.3.0	Butler et al., 2025	https://cran.r-project.org/web/packages/Seurat/index.html
SeuratObject v5.1.0	Hoffman et al., 2025	https://cran.r-project.org/web/packages/SeuratObject/index.html
MAST v1.32.0	https://doi.org/10.1186/s13059-015-0844-5	https://github.com/RGLab/MAST
Giotto v4.2.2	https://doi.org/10.1186/s13059-021-02286-2	https://github.com/drieslab/Giotto
ACAT v0.9.1	Liu, 2018	https://github.com/yaowuliu/ACAT
CARD v3.0-5	https://doi.org/10.1038/s41587-022-01273-7	https://github.com/YMa-lab/CARD

ggplot2 v3.5.2	Wickham et al., 2025	https://cran.r-project.org/web/packages/ggplot2/index.html
ggrepel v0.9.6	Slowikowski et al., 2024	https://cran.r-project.org/web/packages/ggrepel/index.html
ggpubr v0.6.1	Kassambara, 2025	https://cran.r-project.org/web/packages/ggpubr/index.html
ggbeeswarm v0.7.2	Clarke, 2023	https://cran.r-project.org/web/packages/ggbeeswarm/index.html
pheatmap v1.0.13	Kolde, 2025	https://cran.r-project.org/web/packages/pheatmap/index.html
gridExtra v2.3	Auguie et al., 2025	https://cran.r-project.org/web/packages/gridExtra/index.html
cowplot v1.2.0	Wilke, 2025	https://cran.r-project.org/web/packages/cowplot/index.html
scales v1.4.0	Wickham et al., 2025	https://cran.r-project.org/web/packages/scales/index.html
RcolorBrewer v1.1-3	Neuwirth, 2022	https://cran.r-project.org/web/packages/RColorBrewer/index.html
Matrix v1.7-3	Bates et al., 2025	https://cran.r-project.org/web/packages/Matrix/index.html
effectsize v1.0.1	Ben-Shachar et al., 2025	https://cran.r-

		project.org/web/packages/effectsize/index.html
RANN v2.6.2	Jefferis et al., 2024	https://cran.r-project.org/web/packages/RANN/index.html
plyr v1.8.9	Wickham, 2023	https://cran.r-project.org/web/packages/plyr/index.html
dplyr v1.1.4	Wickham et al., 2023	https://cran.r-project.org/web/packages/dplyr/index.html
reshape2 v1.4.4	Wickham, 2020	https://cran.r-project.org/web/packages/reshape2/index.html
tidyverse v2.0.0	Wickham, 2023	https://cran.r-project.org/web/packages/tidyverse/index.html
jsonlite v2.0.0	Ooms et al., 2025	https://cran.r-project.org/web/packages/jsonlite/index.html
readxl v1.4.5	Wickham et al., 2025	https://cran.r-project.org/web/packages/readxl/index.html
openxlsx v4.2.8	Schauberger et al., 2025	https://cran.r-project.org/web/packages/openxlsx/index.html
data.table v1.17.8	Barrett et al., 2025	https://cran.r-project.org/web/packages/data.table/index.html
deldir v2.0-4	Turner et al., 2024	https://cran.r-project.org/web/packages/deldir/inde

		x.html
patchwork v1.3.1	Pedersen et al., 2025	https://cran.r-project.org/web/packages/patchwork/index.html
anndata v0.12.2	Virshup et al., 2024	https://github.com/scverse/anndata
scanpy v1.11.4	Wolf et al., 2018	https://scanpy.org
Squidpy v1.6.5	Palla et al., 2022	https://github.com/scverse/squidpy
Scvi-tools v1.2.0	Gayoso et al., 2022	https://scvi-tools.org
Pandas v2.2.2	McKinney et al., 2010	https://pandas.pydata.org
Scipy v1.16.1	Virtanen et al., 2020	https://scipy.org/
Matplotlib v3.10.0	Hunter et al., 2007	https://matplotlib.org
Seaborn v0.13.2	Waskom et al., 2021	https://seaborn.pydata.org/

EXPERIMENTAL MODEL AND SUBJECT DETAILS

Human subsets

Patients at Mount Sinai Hospital (MSH) were enrolled in the study following Institutional Review Board (IRB) approval (protocol 10-1180). 10-1180 covers the use of patient tissues in a biorepository and allows for prospective collection of blood, urine, and tissue samples from enrolled patients. Formalin-fixed paraffin-embedded (FFPE) blocks from BCG patients were obtained retrospectively from the biorepository and prospectively for patients receiving treatment. For prospective patients, samples were collected on the day of surgery and throughout BCG immunotherapy. Due to IRB limits on the collection, blood and urine samples were taken at the first dose, third dose, and sixth dose of the induction cycle; at every follow-up cystoscopy; and at the third maintenance cycle dose. Tumor samples were taken at every possible timepoint. BCG naïve was defined as any patient who had yet to receive BCG, regardless of past treatment with other chemotherapies. BCG-unresponsive was defined as any patient with recurrent tumors following at least five of six induction doses of BCG at time of first evaluation.

680

681 **Cell lines**

682 HLA-E+ and Wild-type K562 cell lines were kindly provided by Deepta Bhattacharya and propagated as
683 recently described (Berrien-Elliott et al., 2020). HLA-E+ K562 cells were generated using the AAVS1-
684 EF1a donor plasmid containing the coding sequence for human HLA-E. The K562 were electroporated
685 using a Bio-Rad Gene Pulse electroporation system. HLA-E+ cells were sorted to >98% purity. Bladder
686 cancer cell lines were provided by John Sfakianos: 253J(RRID: CVCL_7935),
687 639V(RRID:CVCL_1048), 5637(RRID: CVCL_0126), J82(RRID: CVCL_0359), KU-19-19(RRID:
688 CVCL_1344), MGHU3(RRID: CVCL_9827), RT4(RRID: CVCL_0036), RT112(RRID: CVCL_1670),
689 SW1710(RRID:CVCL_1721), T24(RRID: CVCL_0554), UMUC3(RRID: CVCL_1783).

690

691 **METHOD DETAILS**

692 **Sample processing**

693 Urine samples from bladder cancer patients were spun down to collect cell-free urine, that was
694 stored at -80C. Tumor tissues obtained from transurethral resections of bladder tumor (TURBT) were
695 placed into RPMI medium immediately after removal and transferred to the laboratory for additional
696 processing. Bladder from radical cystectomies was bivalved; samples of visible tumor were extracted and
697 placed in RPMI medium, and the tumor was transferred to the laboratory for additional processing. Fresh
698 tumor samples underwent a variety of different processing techniques based on the planned experiment.
699 Tumor used for spatial sequencing was placed in a 10 mm x 10 mm cryomold with optimal cutting
700 temperature (OCT) media and frozen down on a thermal block immersed in liquid nitrogen. Tumor
701 tissues were digested using tumor dissociation enzymes (Miltenyi, 130-095-929) and a GentleMACS
702 machine (program 37C_h_TDK_3) at 37C. Mechanically and enzymatically separated tissues were
703 filtered through a 70μM cell strainer and assessed on Countess II (ThermoFisher) for viability and cell
704 numbers.

705

706 **Multiplex Immunohistochemistry**

707 Sections of tumors for immunohistochemical (IHC) staining were taken at a thickness of 3-mm from
708 formalin fixed paraffin-embedded (FFPE) blocks. H&E-stained sections were performed every 5 - 10
709 slices. The Ventana Discovery Ultra (Roche Diagnostics) machine was used to automatically bake,
710 deparaffinize, and condition the slices. The RUO Discovery Universal (v21.00.0019) was used to perform
711 chromagen IHC on sequential slices. Primary antibodies included CD3, HLA-E, NKp46, and NKG2A

and were utilized for staining on NMIBC tumors. All slices followed the same protocol, which included a 60 minute incubation at 37°C; secondary antibodies using OmniMap HRP or NP DISCOVERY (Roche Diagnostics); signal detection using Discovery OmniMap. Nuclear counterstaining with Mayer's hematoxylin; and conversion to high-resolution images via the NanoZoomer S10 Digital slide scanner (Hamamatsu).

Tumor and CD3$^+$ T cell expression and proximity analyses

Prior to analysis, all slides were reviewed and regions of interest were annotated by a board-certified pathologist (R.B.). Tissue artifacts, including torn, folded, and damaged tissue, were excluded from any analyses. The HALO^{TM} (Indica Labs, Inc.) digital image analysis platform, a semi-automated platform using machine learning to segment and label stained sections, was utilized for quantitative analyses. Halo AI^{TM} and train-by-example classification, segmentation, and random forest classification was used to separate chromogenic stains and generate tabular data for downstream analysis. Slide features of each tumor, including cell lineages (tumor, stroma, and immune) and slide features (such as glass) were characterized. Glass was excluded from all downstream analyese. Classified cell classes were tabulated, and positive staining cells were stratified into expression tertiles (dim, moderate, and bright). Calibration for intensity expression was performed using tonsil tissues from healthy human tonsil. In addition to cell counts, total surface area (mm^2) was recorded to facilitate density calculations. Statistical analyses were performed using Python 3.8.1.

Proximity Ligation Assay: sample preparation

The NaveniFlex^{TM} Proximity Ligation Assay (PLA) was performed according to the manufacturer's instructions using NaveniFlex Tissue MR ATTO647N (Navinci, Sweden). PLA was performed on sections of tumor taken at a thickness of 3-mm from formalin fixed paraffin-embedded (FFPE) blocks. H&E-stained reviewed with pathologist. Briefly, after deparaffinization, rehydration, and antigen retrieval, slides were blocked with Block NT blocking solution (Navinci, NT.1.100.01) for 60 min at 37 °C in a preheated humidity chamber and then incubated with mouse anti-HLA-E (clone: MEM-E/02, Abcam, 1:200) and rabbit anti-NKG2A (clone: EPR23737-127, Abcam, 1:2000) diluted in Diluent 1 NT solution (Navinci, NB.1.100.02) overnight at 4°C. As negative controls, two (tonsillectomy) slides were incubated in antibody diluent with only one primary antibody each. After washing, the slides were incubated with the PLA probes corresponding to the primary antibodies using anti-mouse Navenibody M1 NT (Navinci, NB.1.100.06) and anti-rabbit Navenibody R2 NT (NB.1.100.07) in Diluent 2 NT

744 solution (Navinci, Navinci, NF.1.100.03) for 60 min at 37 °C. Slides were then processed for ligation
745 using reaction 1 reagent containing Buffer 1 NT (Navinci, NB.2.100.17) and Enzyme 1 NT (Navinci,
746 NF.2.100.11) and subsequently reaction 2 reagent containing Buffer 2 NT (NT.2.100.01) and Enzyme 2
747 NT (Navinci, NF.2.100.15) and incubated for 30 min at 37 °C and 90 min at 37 °C, respectively. The
748 slides were washed and incubated with post-block NT reagent (Navinci, NF.1.100.01) in post-block
749 supplement NT (Navinci, NT.2.100.04) for 30 min at 37 °C, then processed for detection, counter-stained
750 with DAPI, and mounted with coverslips using Prolong Gold Antifade reagent (Invitrogen, P36930).

751

752 **Proximity Ligation Assay: images capture**

753 Images were captured at the Microscopy and Advanced Bioimaging Core of the Icahn School of
754 Medicine at Mount Sinai. A Leica DMi8 (Leica Microsystems, Germany) was equipped with a HC PL
755 APO CS 10x/0.4 (Part Number 506285; Leica Microsystems, Germany) objective lens. A SpectraX
756 fluorescence illuminator (Lumencor, Oregon, USA) with multiple narrow-band light emitting diodes
757 provided illumination (LEDs used: 395/25nm for DAPI, 470/24nm for autofluorescence channel, and
758 640/30nm for Navinci signal). The microscope and light source were controlled by LAS X software,
759 version 3.7.5.24914 (Leica Microsystems, Germany). For fluorescence excitation, the following
760 illumination settings were used: a 395nm LED set to 50% (147mW at the SpectraX output port) for DAPI
761 signal, captured at 20 milliseconds of exposure; a 470nm LED set to 44% (86mW), captured at 70
762 milliseconds for an autofluorescence channel; and a 640nm LED set to 100% (231mW), captured at 150
763 milliseconds for the target signal. A multi-band pass filter set (Part Number 11525366; Leica
764 Microsystems, Germany) was used to separate fluorophore emission (Dichroic 415/490/570/660nm;
765 Emission bands: 430/35, 515/40, 595/40, 720/100nm). Images were captured using a Leica DFC9000GT
766 monochrome camera set to 12-bit depth, 2x2 (4-pixel) binning and “Low Noise” Gain mode. Images were
767 captured in montage at 10% overlap, merged (“Smooth” blending option) and then saved in the
768 proprietary LIF ("Leica Image File") format before being converted to IMS (Imaris) format for analysis.

769

770 **Proximity Ligation Assay: images analyses**

771 Image analysis was performed using Imaris software 10.1.1 (Oxford Instruments, Concord MA). A
772 surface for the green background channel was created using the surface creation wizard with the
773 following parameters – Enable Region Of Interest = false, Enable Region Growing = false, Enable

Tracking = false, Enable Classify = false, Enable Shortest Distance = false, Enable Smooth = true, Surface Grain Size = 2.00 µm, Enable Eliminate Background = false, Active Threshold = true, Enable Automatic Threshold = false, Manual Threshold Value = 1900, Active Threshold B = false. Masked channels were created by subtracting the intensities within the green surface from the blue and far-red channels: the mask intensity was set to 0 for inside the green surface while the outside was set to the original channel's value. A new surface was created using the surface creation wizard for the masked far-red channel using the following parameters – Enable Region Of Interest = false, Enable Region Growing = false, Enable Tracking = false, Enable Classify = false, Enable Shortest Distance = false, Enable Smooth = true, Surface Grain Size = 2.00 µm, Enable Eliminate Background = false, Active Threshold = true, Enable Automatic Threshold = false, Manual Threshold Value = 1600, Active Threshold B = false. An area filter was applied to this far-red surface to remove surfaces whose area was larger than 50um^2. A DAPI surface was created using surface creation wizard with the parameters – Enable Region Of Interest = false, Enable Region Growing = true, Enable Tracking = false, Enable Classify = false, Enable Shortest Distance = true, Enable Smooth = true, Surface Grain Size = 2.00 µm, Enable Eliminate Background = true, Diameter Of Largest Sphere = 7.50 µm, Active Threshold = true, Enable Automatic Threshold = false, Manual Threshold Value = 10, Active Threshold B = false, Region Growing Estimated Diameter = 6.00 µm, Region Growing Morphological Split = false, Filter Seed Points = "Quality" above 60.0, Filter Surfaces = "Number of Voxels Img=1" between 10.0 and 500, to obtain individual nulcei within the field of views. Finally, a fourth surface was created by applying the filter – Overlapped Area to Surfaces (Minimum = 0.050 um^2, Maximum = false) to obtain the DAPI surfaces that were in contact with the far-red channel. The counts of total number of nuclei and nuclei overlapping with the masked far-red surfaces were extracted from the statistics tab of Imaris.

Protein concentration measurement

OLINK Proteomics®- inflammation panel and immuno-oncology 92 assays panel were used to profile cell-free urine supernatant from the Mount Sinai and the Aarhus university cohorts, respectively. Cell-free urine supernatant and serum samples were randomized in a 96-well plate. and incubated overnight alongside negative controls with an incubation mix (incubation solution, incubation stabilizer, A-probes, and B-probes) at 4°C. Samples were then incubated with an extension mix (High purity water, PEA solution, PEA enzyme, PCR polymerase) for 5 min and placed on a thermal cycler. Following the thermal cycler, samples were incubated with a detection mix (detection solution, High purity water, detection enzyme, PCR polymerase) and transferred to a chip. Primers were loaded onto the chip, and the chip was

profiled using the Fluidigm IFC controller HX with the Fluidigm Biomark Reader. Data were normalized using extension and interplate controls and a correction factor. The resulting data were reported in normalized protein expression (NPX) units on a log2 scale. In order to determine the suitable statistical test, a Shapiro-Wilk's test was used to assess for normality, and a Kruskal-Wallis test was used in every instance in which one or both samples were not normally distributed. An independent T-test was used in the event both samples were normally distributed. All statistically significant p values were then used to assess adjusted p values via the Benjamini-Hochberg correction, with an alpha of 0.05. All statistically significant genes between the BCG naïve and sixth induction dose time points are shown.

IFN-γ stimulation of tumor cells

Cell lines and CD45- isolated primary tumor cells were incubated in media optimized for high viability for 72 hours (RPMI-1640 supplemented with 20% fetal bovine serum). Tumor cells were expanded until they were confluent in two T175 flasks. Following expansion, cells were cultured in 100 ng / mL of IFN-γ for a total of 24 hours in a 24 well plate. Following co-culture, cell lines were trypsinized and primary tumors were gently removed from the solid phase by a cell scraper. HLA-E and PD-L1 levels were assessed via Flow Cytometry. Cells were stained in 4C FACS buffer (phosphate-buffered saline (PBS) with 2% heat-inactivated FBS and EDTA 2 mM) for 30 minutes. Subsequently, cells were washed in PBS, incubated for 20 minutes in a viability dye, washed again with PBS, and resuspended in 2% paraformaldehyde. The experiment was performed in triplicate, with three readouts per cell line per experimental condition. Samples were acquired with an LRS-Fortessa (BD Biosciences), and data were analyzed using the CytoBank software. When staining for HLA-E, cells were first stained 20 minutes with HLA-E prior to staining with additional PD-L1. In CytoBank, several gates were applied to generate the final dataset. A live/dead gate was applied, followed by a gate to remove doublets and isolate singlets. Lastly, the data was arcsinh transformed prior to analysis.

Single-cell RNA sequencing: Data preprocessing

Single-cell RNA sequencing (scRNA-seq) analysis was performed using Python and R. After loading, genes expressed in fewer than three cells were excluded from later analyses. Cells with < 200 or > 8000 unique genes, as well as cells containing >20% mitochondrial gene transcripts, were discarded. Doublet cells were screened by scrublet, where expected doublet rate was set at 5.0%, and detected doublet rate was 0.0%. Subsequent data was preprocessed with the Scanpy package and normalization was performed by dividing feature counts for each cell by total counts for that cell, scaling by a factor of 10,000, and

natural log transformation. Next, scvi model was set up to correct batch-effects. Then we performed scaling and principal component analysis (PCA) on the batch-corrected data. Using the first 50 principal components (PCs), graph-based clustering and UMAP dimensionality reduction was performed to reveal 16 cell clusters. Clusters were assigned major cell types by UCDeconvolve. Myeloid cells or CD8 T cells and NK cells were further reclustered and reannotated with Seurat. Subcluster-specific marker genes were identified using the FindAllMarkers function, and marker genes with a natural-log fold change (FC) > 0.25 and expressed in >= 25% of cells were used to annotate cell cluster identities based on known cell type markers [38-40]: CD8 T cells (*CD8A*^{high}, *CD3G*^{high}), CD4 T cells (*CD4*^{high}, *CD3G*^{high}), Regulatory T cells (*CD4*^{high}, *CD3G*^{high}, *FOXP3*^{high}), NK cells *(CD8A*^{low}, *CD3G*^{low}, *GNLY*^{high}), monocytes (*CD14*^{high}, *LYZ*^{high}, *FCGR3A*^{high}), macrophages (*C1QA*^{high}), DC1 *(CLEC9A*^{high}, *XCL1*^{high}), DC2 *(FCER1A*^{high}, *CD1C*^{high}*)*, mReg DCs *(LAMP3*^{high}). All scRNAseq analyses were performed using distinct samples without repeated measurements.

Single-cell RNA sequencing: Subclustering analyses

We performed subclustering analysis on 18,520 bladder tumor cells using Seurat v5 workflow. We integrated tumor cell transcriptomes across samples using Canonical Correlation Analysis (CCA) integration with the IntegrateLayers() function (dimensional reduction for correction = pca). Leiden clustering (resolution = 0.4) was applied to the shared nearest neighbors (SNN) (dims = 1:10). This resulted in the identification of 9 heterogeneous tumor subclusters, distinctly separated on the UMAP plot. Each subcluster was profiled by the expression of tumor marker genes (EPCAM, UPK2) and cytokines (CXCL1, CXCL2, CXCL3, IFNGR1, etc.). Subcluster B1 was removed from further analysis as it was identified as normal bladder cells with low EPCAM (tumor-related marker genes) , and subcluster B8 was removed due to high PTPRC expression, indicating a high presence of immune cells (CD45+). Differentially expressed gene (DEG) analysis (MAST, R version 1.2.1) [42] and enrichment pathway analysis [43] further characterized the subclusters, highlighting their distinct biological profiles (Figure 2).

NK cells were similarly subclustered using Seurat (resolution=0.5, dims=1:10). 5 subclusters were revealed by unsupervised clustering. Using TransferData() in Seurat, we mapped our NK cells to publicly available subclustered NK cell data: Rebuffet et al. 2024 (NK1A, NK1B, NK1C, NK2, NK3, NKint), and Netskar et al. 2024 (NK of group 1 through 6) for comparison.

Spatial transcriptomics: data generation

Spatial transcriptomic data were generated by Visium Spatial Gene Expression. We obtained eight spatial sections consisting of four pre-BCG and four post-BCG samples after review of samples by a board-certified pathologist. Sequencing data were aligned on GRCh38 and quantified using the Space Ranger Software Suite (version 1.0, 10x Genomics). The data were processed to characterize major cell types and their spatial patterns using Giotto workflow [44]. Briefly, low quality spots (number of expressed genes lower than or equal to 100), and lowly expressed genes (expressed in less than 10 spots) were removed. The raw counts were log2(x+1) transformed, batch-adjusted and filtered for spot wise features using Pearson residuals approach by Lause et al [45]. The spatial network of nearest spots by Delaunay triangulation was calculated to identify spatially co-expressed genes in neighboring spots via BinSpect-kmeans algorithm [44], and distinct spatial domains by Hidden Markov Random Field (HMRF) model [44]. Then, transcriptomes from different spatial samples were integrated by Harmony using the top 10 principal components from each samples to identify the clusters [46]. The integrated clusters were identified by Leiden clustering [44] with at clustering resolution (γ) at 0.8 using *FindNeighbors()* and *FindClusters()* functions in Seurat R package. Subsequently, we identified 12 spatial clusters to profile the spatial transcriptomic landscape. Differentially expressed genes (DEGs) between $KLRC1^{+}$ versus $KLRC1^{-}$ cells were found using the FindMarkers function from the Seurat R package, where cells with KLRC1 expression greater than 0 in the RNA assay were labeled as $KLRC1^{+}$.

Spatial transcriptomics: Identification of HLA-E high/low tumor subsets

As HLA-E expressions are not specific to tumors and HLA-E high/low tumor markers have not been established, we designed a workflow to first infer the voxels with tumor presence, then identify HLA-E expressing tumors to scrutinize the HLA-E high/low tumors. To this end, we performed a cell type deconvolution on the spatial transcriptomes. Cell Atlas Reconstruction from Spatially mapped Data (CARD) method [47]. CARD is a computational approach that reconstructs cell-type-specific expression profiles from spatially mapped transcriptomic data, facilitating the estimation of cell-type proportions within tissue sections. This involved provision of reference single-cell transcriptomes with tumor cells grouped by $HLA\text{-}E^{high}$ and $HLA\text{-}E^{low}$ tumor labels (high: HLA-E gene expression> 0, low: HLA-E=0). These tumor labels were utilized as the inputs to calculate the relative abundances of the tumor subsets on the spatial voxels by CARD. To further scrutinize the detection of HLA-E high tumors in the spatial transcriptome (ST) data, we applied additional thresholds to require voxels with i) high HLA-E expressions, and ii) highly abundant HLA-E high tumor/stromal cells as inferred by CARD [47]. Per

section, high HLA-E expression voxels were identified as those with HLA-E expression values greater than zero and a z-score of inferred HLA-E^{high} tumor/stromal cell abundance > 1.645 (90% confidence). Conversely, low HLA-E expression voxels were identified as those with an absence of HLA-E expression (HLA-E expression equal to zero) and a z-score of inferred HLA-E^{low} tumor/stromal cell abundance > 1.645 (90% confidence). Similarly, we detected high confidence voxels with NK cells, CD8 T-cells and Treg cells by further applying the abundance z-score > 1.645 for further analyses.

Spatial transcriptomics: Proximity analysis between different cell types

We evaluated the proximity between different immune subsets (NK, CD8+ T, and regulatory T (Treg) cells) and HLA-E$^{high/low}$ tumor cells to observe if distinct cytotoxic immune micro-environments are present, conditioned on tumoral HLA-E expression status. Upon identifying high confidence voxels with HLA-E$^{high/low}$ tumor/stromal cells and the immune cell types, we calculated the pairwise Euclidean distances between the tumor/stromal cells and each immune cell type. To retrieve actual distance between voxels, the matrix was refined using the computeCellDistance function from the CellChat v2 library in R to incorporate the scale factors in the spatial coordinates [48]. For each voxel with HLA-E$^{high/low}$ tumor/stromal cell presence, its overall distance to an immune cell type was calculated as the mean distance over the 10 nearest neighboring voxels with the respective immune cell presence. These distances were summarized across each section by taking the average over all HLA-E$^{high/low}$ tumor/stroma voxels, yielding the overall proximity with each immune cell type per section. These overall proximity values were compared between pre-BCG and post-BCG groups by Wilcoxon Rank-sum test.

Spatial transcriptomics: Cell type enrichment across spatial clusters

We tested if each pan-section cluster shows enriched presence of distinct cell populations and subsets as characterized by the scRNA-seq. To this end, for each section, we leveraged the inferred abundances of different cell types in the spatial voxels by CARD, and tested if a cell type has significantly higher abundances in each pan-section cluster than the other voxels by Wilcoxon Rank-sum test. Then, the overall enrichments of each cell type within pre-BCG or post-BCG group were summarized by combining the Wilcoxon test p-value across the sections via aggregated Cauchy association test (ACAT). The enriched cell types per pan-section cluster in pre-BCG or post-BCG group were called with ACAT summarized FDR < 0.05 and number of sections with significant enrichments (Wilcoxon FDR < 0.05) > 1.

In situ hybridization and targeted RNA sequencing

FFPE sections from 40 retrospective NMIBC cases were obtained from the institutional biorepository and used for targeted RNA sequencing. RNA was extracted from five and ten μm sections. HTG EdgeSeq lysis buffer was added to lyse and permeabilize the samples. Nuclease protection probes (NPPs) were added to the lysed samples and hybridized to the target mRNA. A nuclease was added to digest non-hybridized mRNA and excess NPPs. The nuclease digestion reaction was finalized with a termination solution followed by heat-mediated denaturation of the enzyme. Each sample was used as a template for PCR reactions with specially designed primers. Each primer contains a unique barcode that is used for sample identification and multiplexing. Samples were analyzed simultaneously on an Illumina sequencing platform to prepare the library. All samples and controls were quantified in triplicates. No template control (NTC) reactions were made for each master mix used during the qPCR process to test the absence of a probe or qPCR contamination. Molecular-grade water was used in place of a test sample in the NTC reactions using the same volume as the template. Sufficient concentration of sample for library pooling, appropriate dilution for the library pool, and volume of denaturation reagents to add to the library were determined by HTG library calculator. 2N NaOH and heat (98C, 4 minutes) were used for library denaturation. The denatured library was loaded into the well of the NextSeq sequencing cartridge. Sequencing was performed using an Illumina NextSeq sequencer. The sequencing data on mRNA expression of target genes were imported into HTG EdgeSeq parser software. HTG biostatistics department performed quality control analyses and normalized the data. Data were returned from the sequencer as demultiplexed FASTQ files with four files per assay well. The HTG EdgeSeq parser software aligned the FASTQ files to the probe list and collated the data.

***mRNA in situ* hybridization: Gene set enrichment analysis**

gene set enrichment analysis (GSEA) was performed on the targeted RNA sequencing data. Specifically, we used paired patient samples before and after BCG exposure in the BCG recurrent patient population only. We used custom gene sets, as well as all Hallmark gene sets from the Broad Institute's MSigDB, as inputs for the enrichment analysis [49]. Statistical significance was set at $p < 0.05$. All gene sets found to be statistically significant were evaluated for leading-edge genes, defined as the genes that contribute most to the enrichment score and associated p-value. The leading-edge genes from statistically significant gene sets in the GSEA were collated and used to assess for group differences between the paired HTG patient samples. We performed these analyses specifically on the BCG-recurrent cohort. Prior to any analyses, a Shapiro-Wilk test, chosen for suitability in small sample sizes, was used to assess for normality [50]. All

samples with $p < 0.05$ were considered not normally distributed, and a Kruskal-Wallis test was performed to assess for group differences [51]. All other samples were assessed using an independent T-test. Genes with statistically significant differences between the BCG naïve and the BCG-unresponsive populations were then visualized on radar plots.

Tumor-infiltrating lymphocytes (TILs) Expansion

TILs were expanded by seeding single cells tumor dissociate at 10^5 cells/well in 48-well Costar® flat-bottom plates (Corning Inc., NY) in complete TIL medium, consisting of RPMI 1640 with L-glutamine (Corning Inc., NY), 10% human AB serum (MiliporeSigma, MO), 1% nonessential amino acids (Thermo Fisher Scientific, MA), 1% sodium pyruvate (Thermo Fisher Scientific, MA), 1% penicillin/streptomycin (Thermo Fisher Scientific, MA), and 3000 IU/ml interleukin-2 (Proleukin®, kindly provided by Clinigen). Cells were stimulated using 25 µl ImmunoCult™ Human CD3/CD28/CD2 T Cell Activator (STEMCELL Technologies, Vancouver, BC) and seeded on 1.5 x 10^6 feeder cells, which were derived from healthy control PBMCs (New York Blood Center, NY) and irradiated at 50 Gy. TILs were incubated at 37°C, 5% CO_2 and maintained by replacement with fresh complete TIL medium every 2 days. After three weeks, expanded TIL lines were frozen in 10% DMSO (MiliporeSigma, MO), 90% FBS (MiliporeSigma, MO) and stored in LN_2.

TIL Co-culture with K562s Expressing Checkpoints

For co-culture and surface stain of PD-L1 and HLA-E, three separate K562 tumor lines of K562 cells were generated using 400 ng/ml of IFN-γ for 72 hours: WT, E+, and E+/PD-L1+ lines. Two separate rounds of stimulation were performed on K562 tumors after reaching steady-state expansion. First, K562 tumors were co-cultured at a concentration of 0.5 X 10^6 viable cells / mL with 200 and 400 ng / mL of IFN-γ in R10 media in order to assess the induction of HLA-E and PD-L1 with high doses of IFN-γ. At every 24-hour interval, cell concentration and viability were assessed using a hemocytometer, and K562 tumors were split to a concentration of 0.5 X 10^6 live cells / mL. At 72 hours of incubation, cells were spun at 1650 RPM, washed with FACS buffer (PBS, 5% FBS, 0.2% EDTA), resuspended in 5 mL of FACS buffer, and assessed for concentration and viability. 0.5 X 10^6 live cells were removed, and spun to remove the FACS buffer. K562 tumors were first incubated with zombie near infrared (NIR) at a dilution of 1 in 1000 for 20 minutes at room temperature. Following the zombie stain, cells were washed in 1 mL of FACS buffer, and incubated with PD-L1 (PE; Biolegend cat #124308), and HLA-E (per-CP CY5.5; Biolegend cat #342609) antibodies in a 1:25 dilution cocktail for 30 minutes on ice in the dark. Cells were

washed again in FACS buffer and suspended in 400µLof fixative buffer (2% paraformaldehyde in PBS). HLA-E and PD-L1 levels were then assessed using flow cytometry.

Tumor-infiltrating lymphocytes (TILs) from four BCG-unresponsive NMIBC patients which had been expanded using the protocol listed above were thawed and seeded at a concentration of 1 X 10^6 live cells / mL in a stimulatory media consisting of ImmunoCult, CD3/CD28 tetramer (25 uL/mL), IL-2 (10 IU/mL), IL-7 (10 ng/mL), and IL-15 (10 ng/mL). Cells were seeded and plated in a 96 round-bottom plate. At days three, five, seven, and nine, 50% of the media was aspirated and replaced with fresh media at twice the initial concentration of cytokines, without CD3/28 tetramer. At day 10, TGF-β, Immunocult, IL-2 (10IU/mL), IL-7 (10ng/mL), IL-15 (10ng/mL), CD3/CD28 tetramer (25µL/mL), TGF-β (5ng/mL)) was provided to stimulate expression of NKG2A on the TILs.

At day 13, the stimulation was complete, and the TILs were co-cultured with combinations of the K562 cells expressing forms of PD-L1 and HLA-E. In total, 12 experimental co-culture conditions were conducted for each patients' TIL sample (n=4): two control wells (ex-vivo, and stimulated with a CD3/28 spike); with K562 WT cells, HLA-E^+ cells, or HLA-E^+ PD-$L1^+$ cells without antibody; TILs in the presence of HLA-E^+ or HLA-E^+PD-$L1^+$ K562s with durvalumab alone, or both durvalumab plus monalizumab; and lastly, TILs and WT K562s in the presence of monalizumab and durvalumab.

TILs were cultured in TIL medium, consisting of RPMI 1640 with L-glutamine (Corning Inc., NY), 10% human AB serum (MiliporeSigma, MO), 1% nonessential amino acids (Thermo Fisher Scientific, MA), 1% sodium pyruvate (Thermo Fisher Scientific, MA), 1% penicillin, streptomycin (Thermo Fisher Scientific, MA). Cultures were performed in 96-well u-bottom plates (Corning Inc., NY). TILs were added to each well at a concentration of at 3 x10^5 cells/condition in TIL medium. K562s were resuspended in TIL medium and added at 5 x 10^4 singe-cell equivalents/condition. Anti-CD28 (BioLegend, CA) was added to each well at 1 µg/ml and anti-CD107a-BV785 (BioLegend, CA) was added to each well at 0.3 µg/ml. Monalizumab was added to the TILs a final concentration of 10 µg/ml, and durvalumab was added to the K562s for a final concentration of 10 µg/ml. TILs and K562s were cultured separately for 20 minutes at 37°C prior to co-culture. The K562s and TILs were then combined, thoroughly resuspended, and gently spun for 5 seconds before being returned to the incubator. Plates were incubated at 37°C and 5% CO_2, and after 1 hour of incubation, 0.5X Brefeldin (BioLegend, CA) and 0.5X Monensin (BioLegend, CA) was added to each tube for a final volume of 500 µl, followed by an additional 15 hours of incubation. At hour 16 plates were spun and supernatant was removed; all samples were washed with 200µLof PBS. Samples were resuspended in 50µLof zombie near infrared (NIR) at a 1:3000 dilition, and incubated for 20 minutes in the dark at room temperature. Samples were washed

again, spun, supernatant was removed, and incubated in 50μLof TruStain FCX, diluted 1:200, for 20 minutes in the dark at 4°C. 50μLof the surface antibody master mix (anti-CD3, -CD8, -CD56, -CD4, -PD-1, -NKG2A) was added at 20 minutes, and returned to the fridge to incubate in the dark at 4°C for 30 more minutes. Plates were washed twice more in FACS buffer, and were suspended in 0.2% FBS FACS buffer for storage until intracellular staining.

12 hours prior to sample acquisition, intracellular staining was performed for IFN-γ. 100 μL of intracellular staining permeabilization wash buffer (BioLegend) was added to each well, the plates were spun, and supernatant discarded. This was performed 2 additional times with 200 μL of permeabilization wash buffer. 50 μL of the intracellular staining antibody mix was added to each well, and the plates were incubated for 20 minutes at 4°C. The plates were washed in 0.2% FBS FACS buffer and resuspended for storage in 0.2% FBS FACS buffer

References

1. Redelman-Sidi, G., Glickman, M.S., and Bochner, B.H. (2014). The mechanism of action of BCG therapy for bladder cancer--a current perspective. Nat Rev Urol *11*, 153-162. 10.1038/nrurol.2014.15.
2. Ranti, D., Bieber, C., Wang, Y.S., Sfakianos, J.P., and Horowitz, A. (2022). Natural killer cells: unlocking new treatments for bladder cancer. Trends Cancer. 10.1016/j.trecan.2022.03.007.
3. Sfakianos, J.P., Salome, B., Daza, J., Farkas, A., Bhardwaj, N., and Horowitz, A. (2021). Bacillus Calmette-Guerin (BCG): Its fight against pathogens and cancer. Urol Oncol *39*, 121-129. 10.1016/j.urolonc.2020.09.031.
4. Kamat, A.M., Li, R., O'Donnell, M.A., Black, P.C., Roupret, M., Catto, J.W., Comperat, E., Ingersoll, M.A., Witjes, W.P., McConkey, D.J., and Witjes, J.A. (2018). Predicting Response to Intravesical Bacillus Calmette-Guerin Immunotherapy: Are We There Yet? A Systematic Review. Eur Urol *73*, 738-748. 10.1016/j.eururo.2017.10.003.
5. Li, R., Hensley, P.J., Gupta, S., Al-Ahmadie, H., Babjuk, M., Black, P.C., Brausi, M., Bree, K.K., Fernandez, M.I., Guo, C.C., et al. (2024). Bladder-sparing Therapy for Bacillus Calmette-Guerin-unresponsive Non-muscle-invasive Bladder Cancer: International Bladder Cancer Group Recommendations for Optimal Sequencing and Patient Selection. Eur Urol *86*, 516-527. 10.1016/j.eururo.2024.08.001.
6. Hedgepeth, R.C., Gilbert, S.M., He, C., Lee, C.T., and Wood, D.P., Jr. (2010). Body image and bladder cancer specific quality of life in patients with ileal conduit and neobladder urinary diversions. Urology *76*, 671-675. 10.1016/j.urology.2010.01.087.
7. Muller, G., Butea-Bocu, M., Brock, O., Hanske, J., Pucheril, D., Noldus, J., and Otto, U. (2020). Association between Development of Metabolic Acidosis and Improvement of Urinary Continence after Ileal Neobladder Creation. J Urol *203*, 585-590. 10.1097/JU.0000000000000583.
8. Sharma, P., Hu-Lieskovan, S., Wargo, J.A., and Ribas, A. (2017). Primary, Adaptive, and Acquired Resistance to Cancer Immunotherapy. Cell *168*, 707-723. 10.1016/j.cell.2017.01.017.
9. Morales, A., Eidinger, D., and Bruce, A.W. (1976). Intracavitary Bacillus Calmette-Guerin in the treatment of superficial bladder tumors. J Urol *116*, 180-183. 10.1016/s0022-5347(17)58737-6.
10. Morales, A. (2017). BCG: A throwback from the stone age of vaccines opened the path for bladder cancer immunotherapy. Can J Urol *24*, 8788-8793.
11. Kates, M., Matoso, A., Choi, W., Baras, A.S., Daniels, M.J., Lombardo, K., Brant, A., Mikkilineni, N., McConkey, D.J., Kamat, A.M., et al. (2020). Adaptive Immune Resistance to Intravesical BCG in Non-Muscle Invasive Bladder Cancer: Implications for Prospective BCG-Unresponsive Trials. Clin Cancer Res *26*, 882-891. 10.1158/1078-0432.CCR-19-1920.
12. Pfail, J.L., Katims, A.B., Alerasool, P., and Sfakianos, J.P. (2021). Immunotherapy in non-muscle-invasive bladder cancer: current status and future directions. World J Urol *39*, 1319-1329. 10.1007/s00345-020-03474-8.
13. Balar, A.V., Kamat, A.M., Kulkarni, G.S., Uchio, E.M., Boormans, J.L., Roumiguie, M., Krieger, L.E.M., Singer, E.A., Bajorin, D.F., Grivas, P., et al. (2021). Pembrolizumab monotherapy for the treatment of high-risk non-muscle-invasive bladder cancer unresponsive to BCG (KEYNOTE-057): an open-label, single-arm, multicentre, phase 2 study. Lancet Oncol *22*, 919-930. 10.1016/S1470-2045(21)00147-9.
14. Necchi, A., Roumiguie, M., Kamat, A.M., Shore, N.D., Boormans, J.L., Esen, A.A., Lebret, T., Kandori, S., Bajorin, D.F., Krieger, L.E.M., et al. (2024). Pembrolizumab monotherapy for high-risk non-muscle-invasive bladder cancer without carcinoma in situ and unresponsive to BCG (KEYNOTE-057): a single-arm, multicentre, phase 2 trial. Lancet Oncol *25*, 720-730. 10.1016/S1470-2045(24)00178-5.

15. van Montfoort, N., Borst, L., Korrer, M.J., Sluijter, M., Marijt, K.A., Santegoets, S.J., van Ham, V.J., Ehsan, I., Charoentong, P., Andre, P., et al. (2018). NKG2A Blockade Potentiates CD8 T Cell Immunity Induced by Cancer Vaccines. Cell *175*, 1744-1755 e1715. 10.1016/j.cell.2018.10.028.
16. Andre, P., Denis, C., Soulas, C., Bourbon-Caillet, C., Lopez, J., Arnoux, T., Blery, M., Bonnafous, C., Gauthier, L., Morel, A., et al. (2018). Anti-NKG2A mAb Is a Checkpoint Inhibitor that Promotes Anti-tumor Immunity by Unleashing Both T and NK Cells. Cell *175*, 1731-1743 e1713. 10.1016/j.cell.2018.10.014.
17. Salomé, B., Sfakianos, J.P., Ranti, D., Daza, J., Bieber, C., Charap, A., Hammer, C., Banchereau, R., Farkas, A.M., Ruan, D.F., et al. (2022). NKG2A and HLA-E define a novel alternative immune checkpoint axis in bladder cancer. Cancer Cell *40*, 1-17. 10.1016/j.ccell.2022.08.005.
18. Kamiya, T., Seow, S.V., Wong, D., Robinson, M., and Campana, D. (2019). Blocking expression of inhibitory receptor NKG2A overcomes tumor resistance to NK cells. J Clin Invest *129*, 2094-2106. 10.1172/JCI123955.
19. Pereira, B.I., Devine, O.P., Vukmanovic-Stejic, M., Chambers, E.S., Subramanian, P., Patel, N., Virasami, A., Sebire, N.J., Kinsler, V., Valdovinos, A., et al. (2019). Senescent cells evade immune clearance via HLA-E-mediated NK and CD8(+) T cell inhibition. Nat Commun *10*, 2387. 10.1038/s41467-019-10335-5.
20. Herbst, R.S., Majem, M., Barlesi, F., Carcereny, E., Chu, Q., Monnet, I., Sanchez-Hernandez, A., Dakhil, S., Camidge, D.R., Winzer, L., et al. (2022). COAST: An Open-Label, Phase II, Multidrug Platform Study of Durvalumab Alone or in Combination With Oleclumab or Monalizumab in Patients With Unresectable, Stage III Non-Small-Cell Lung Cancer. J Clin Oncol, JCO2200227. 10.1200/JCO.22.00227.
21. Barlesi, F., Cho, B.C., Goldberg, S.B., Yoh, K., Zimmer Gelatti, A.C., Mann, H., Gopinathan, A., Bielecka, Z.F., Newton, M., and Aggarwal, C. (2024). PACIFIC-9: Phase III trial of durvalumab + oleclumab or monalizumab in unresectable stage III non-small-cell lung cancer. Future Oncol, 1-11. 10.1080/14796694.2024.2354160.
22. Li, J., Zhou, J., Huang, H., Jiang, J., Zhang, T., and Ni, C. (2023). Mature dendritic cells enriched in immunoregulatory molecules (mregDCs): A novel population in the tumour microenvironment and immunotherapy target. Clin Transl Med *13*, e1199. 10.1002/ctm2.1199.
23. Burr, M.L., Sparbier, C.E., Chan, Y.C., Williamson, J.C., Woods, K., Beavis, P.A., Lam, E.Y.N., Henderson, M.A., Bell, C.C., Stolzenburg, S., et al. (2017). CMTM6 maintains the expression of PD-L1 and regulates anti-tumour immunity. Nature *549*, 101-105. 10.1038/nature23643.
24. Netskar, H., Pfefferle, A., Goodridge, J.P., Sohlberg, E., Dufva, O., Teichmann, S.A., Brownlie, D., Michaelsson, J., Marquardt, N., Clancy, T., et al. (2024). Pan-cancer profiling of tumor-infiltrating natural killer cells through transcriptional reference mapping. Nat Immunol. 10.1038/s41590-024-01884-z.
25. Rebuffet, L., Melsen, J.E., Escaliere, B., Basurto-Lozada, D., Bhandoola, A., Bjorkstrom, N.K., Bryceson, Y.T., Castriconi, R., Cichocki, F., Colonna, M., et al. (2024). High-dimensional single-cell analysis of human natural killer cell heterogeneity. Nat Immunol. 10.1038/s41590-024-01883-0.
26. Vivier, E., Rebuffet, L., Narni-Mancinelli, E., Cornen, S., Igarashi, R.Y., and Fantin, V.R. (2024). Natural killer cell therapies. Nature *626*, 727-736. 10.1038/s41586-023-06945-1.
27. Chang, S.S., Boorjian, S.A., Chou, R., Clark, P.E., Daneshmand, S., Konety, B.R., Pruthi, R., Quale, D.Z., Ritch, C.R., Seigne, J.D., et al. (2016). Diagnosis and Treatment of Non-Muscle Invasive Bladder Cancer: AUA/SUO Guideline. J Urol *196*, 1021-1029. 10.1016/j.juro.2016.06.049.

28. Cristescu, R., Mogg, R., Ayers, M., Albright, A., Murphy, E., Yearley, J., Sher, X., Liu, X.Q., Lu, H., Nebozhyn, M., et al. (2018). Pan-tumor genomic biomarkers for PD-1 checkpoint blockade-based immunotherapy. Science *362*. 10.1126/science.aar3593.
29. Wang, L., Sfakianos, J.P., Beaumont, K.G., Akturk, G., Horowitz, A., Sebra, R.P., Farkas, A.M., Gnjatic, S., Hake, A., Izadmehr, S., et al. (2021). Myeloid Cell-associated Resistance to PD-1/PD-L1 Blockade in Urothelial Cancer Revealed Through Bulk and Single-cell RNA Sequencing. Clin Cancer Res. 10.1158/1078-0432.CCR-20-4574.
30. Strandgaard, T., Nordentoft, I., Birkenkamp-Demtroder, K., Salminen, L., Prip, F., Rasmussen, J., Andreasen, T.G., Lindskrog, S.V., Christensen, E., Lamy, P., et al. (2023). Field Cancerization Is Associated with Tumor Development, T-cell Exhaustion, and Clinical Outcomes in Bladder Cancer. Eur Urol. 10.1016/j.eururo.2023.07.014.
31. Strandgaard, T., Lindskrog, S.V., Nordentoft, I., Christensen, E., Birkenkamp-Demtröder, K., Andreasen, T.G., Lamy, P., Kjær, A., Ranti, D., Wang, Y.A., et al. (2022). Elevated T-cell Exhaustion and Urinary Tumor DNA Levels Are Associated with Bacillus Calmette-Guérin Failure in Patients with Non–muscle-invasive Bladder Cancer. European Urology. https://doi.org/10.1016/j.eururo.2022.09.008.
32. Spranger, S., Spaapen, R.M., Zha, Y., Williams, J., Meng, Y., Ha, T.T., and Gajewski, T.F. (2013). Up-regulation of PD-L1, IDO, and T(regs) in the melanoma tumor microenvironment is driven by CD8(+) T cells. Sci Transl Med *5*, 200ra116-200ra116. 10.1126/scitranslmed.3006504.
33. Rooney, M.S., Shukla, S.A., Wu, C.J., Getz, G., and Hacohen, N. (2015). Molecular and genetic properties of tumors associated with local immune cytolytic activity. Cell *160*, 48-61. 10.1016/j.cell.2014.12.033.
34. Ribas, A. (2015). Adaptive Immune Resistance: How Cancer Protects from Immune Attack. Cancer Discov *5*, 915-919. 10.1158/2159-8290.Cd-15-0563.
35. Grasso, C.S., Tsoi, J., Onyshchenko, M., Abril-Rodriguez, G., Ross-Macdonald, P., Wind-Rotolo, M., Champhekar, A., Medina, E., Torrejon, D.Y., Shin, D.S., et al. (2020). Conserved Interferon-γ Signaling Drives Clinical Response to Immune Checkpoint Blockade Therapy in Melanoma. Cancer Cell *38*, 500-515.e503. 10.1016/j.ccell.2020.08.005.
36. Gocher, A.M., Workman, C.J., and Vignali, D.A.A. (2022). Interferon-γ: teammate or opponent in the tumour microenvironment? Nat Rev Immunol *22*, 158-172. 10.1038/s41577-021-00566-3.
37. Bisiaux, A., Thiounn, N., Timsit, M.O., Eladaoui, A., Chang, H.H., Mapes, J., Mogenet, A., Bresson, J.L., Prié, D., Béchet, S., et al. (2009). Molecular analyte profiling of the early events and tissue conditioning following intravesical bacillus calmette-guerin therapy in patients with superficial bladder cancer. J Urol *181*, 1571-1580. 10.1016/j.juro.2008.11.124.
38. Zhang, X., Lan, Y., Xu, J., Quan, F., Zhao, E., Deng, C., Luo, T., Xu, L., Liao, G., Yan, M., et al. (2019). CellMarker: a manually curated resource of cell markers in human and mouse. Nucleic Acids Res *47*, D721-d728. 10.1093/nar/gky900.
39. Glass, D.R., Tsai, A.G., Oliveria, J.P., Hartmann, F.J., Kimmey, S.C., Calderon, A.A., Borges, L., Glass, M.C., Wagar, L.E., Davis, M.M., and Bendall, S.C. (2020). An Integrated Multi-omic Single-Cell Atlas of Human B Cell Identity. Immunity *53*, 217-232.e215. 10.1016/j.immuni.2020.06.013.
40. Magri, G., Comerma, L., Pybus, M., Sintes, J., Lligé, D., Segura-Garzón, D., Bascones, S., Yeste, A., Grasset, E.K., Gutzeit, C., et al. (2017). Human Secretory IgM Emerges from Plasma Cells Clonally Related to Gut Memory B Cells and Targets Highly Diverse Commensals. Immunity *47*, 118-134.e118. 10.1016/j.immuni.2017.06.013.
41. Hao, Y., Stuart, T., Kowalski, M.H., Choudhary, S., Hoffman, P., Hartman, A., Srivastava, A., Molla, G., Madad, S., and Fernandez-Granda, C. (2024). Dictionary learning for integrative, multimodal and scalable single-cell analysis. Nature biotechnology *42*, 293-304.

42. Finak, G., McDavid, A., Yajima, M., Deng, J., Gersuk, V., Shalek, A.K., Slichter, C.K., Miller, H.W., McElrath, M.J., and Prlic, M. (2015). MAST: a flexible statistical framework for assessing transcriptional changes and characterizing heterogeneity in single-cell RNA sequencing data. Genome biology *16*, 1-13.
43. Liberzon, A., Subramanian, A., Pinchback, R., Thorvaldsdóttir, H., Tamayo, P., and Mesirov, J.P. (2011). Molecular signatures database (MSigDB) 3.0. Bioinformatics *27*, 1739-1740.
44. Dries, R., Zhu, Q., Dong, R., Eng, C.-H.L., Li, H., Liu, K., Fu, Y., Zhao, T., Sarkar, A., and Bao, F. (2021). Giotto: a toolbox for integrative analysis and visualization of spatial expression data. Genome biology *22*, 1-31.
45. Lause, J., Berens, P., and Kobak, D. (2021). Analytic Pearson residuals for normalization of single-cell RNA-seq UMI data. Genome biology *22*, 1-20.
46. Korsunsky, I., Millard, N., Fan, J., Slowikowski, K., Zhang, F., Wei, K., Baglaenko, Y., Brenner, M., Loh, P.-r., and Raychaudhuri, S. (2019). Fast, sensitive and accurate integration of single-cell data with Harmony. Nature methods *16*, 1289-1296.
47. Ma, Y., and Zhou, X. (2022). Spatially informed cell-type deconvolution for spatial transcriptomics. Nature biotechnology *40*, 1349-1359.
48. Jin, S., Plikus, M.V., and Nie, Q. (2023). CellChat for systematic analysis of cell-cell communication from single-cell and spatially resolved transcriptomics. BioRxiv, 2023.2011. 2005.565674.
49. Liberzon, A., Birger, C., Thorvaldsdóttir, H., Ghandi, M., Mesirov, J.P., and Tamayo, P. (2015). The Molecular Signatures Database (MSigDB) hallmark gene set collection. Cell Syst *1*, 417-425. 10.1016/j.cels.2015.12.004.
50. Shapiro, S.S., and Wilk, M.B. (1965). An Analysis of Variance Test for Normality (Complete Samples). Biometrika *52*, 591-611. 10.2307/2333709.
51. Kruskal, W.H., and Wallis, W.A. (1952). Use of Ranks in One-Criterion Variance Analysis. Journal of the American Statistical Association *47*, 583-621. 10.2307/2280779.

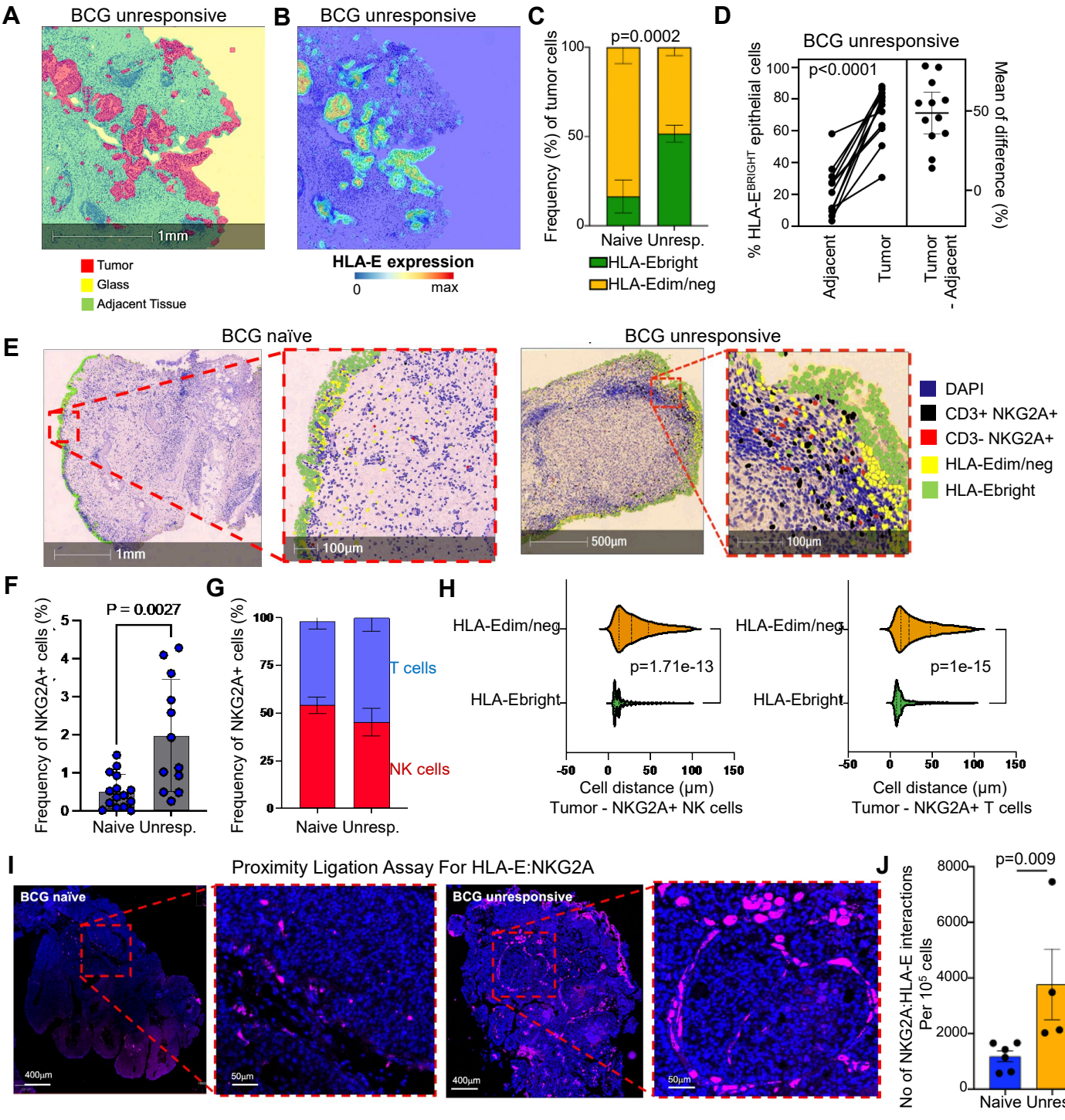

Figure 1

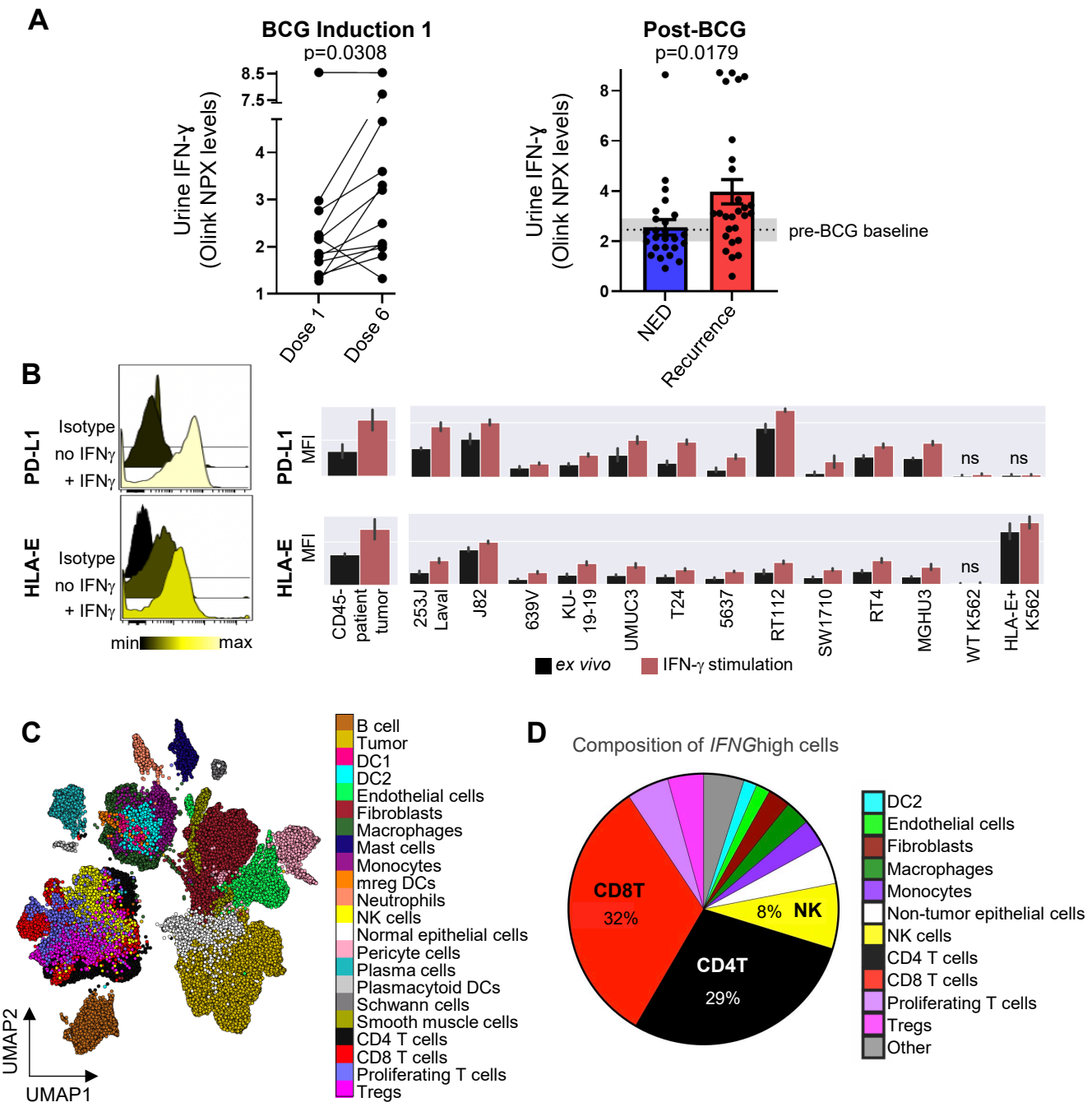

Figure 2

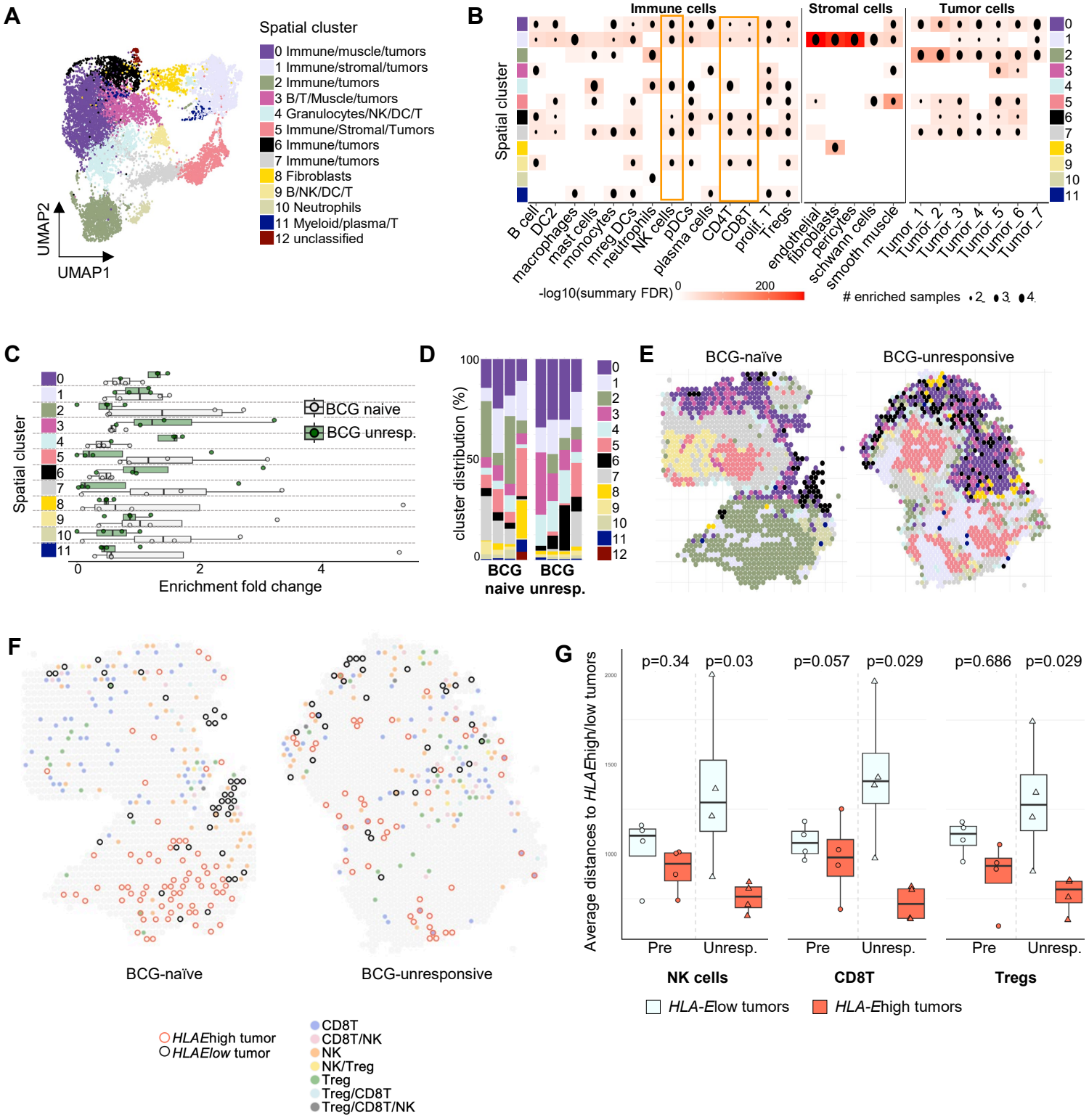

Figure 3

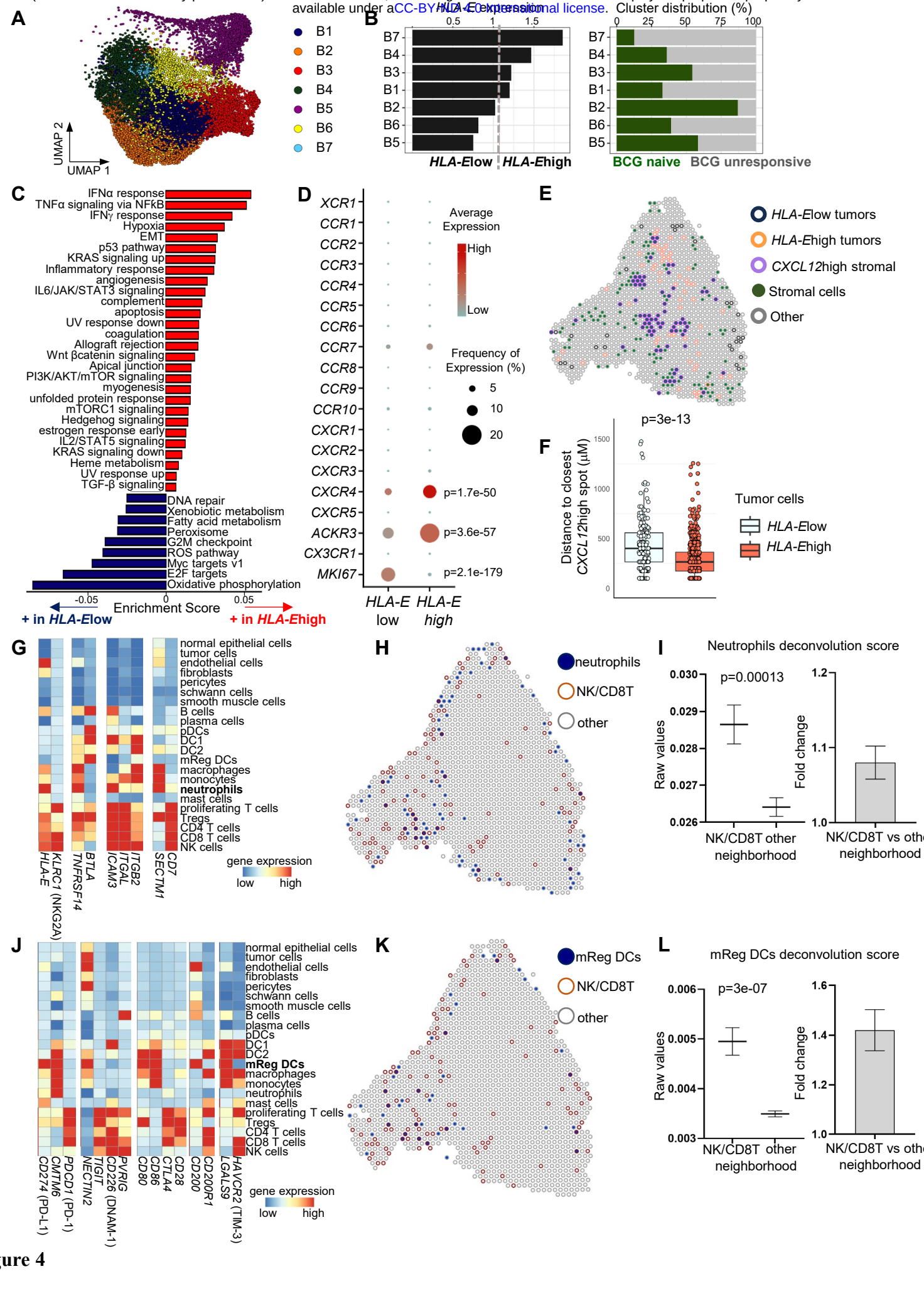

Figure 4

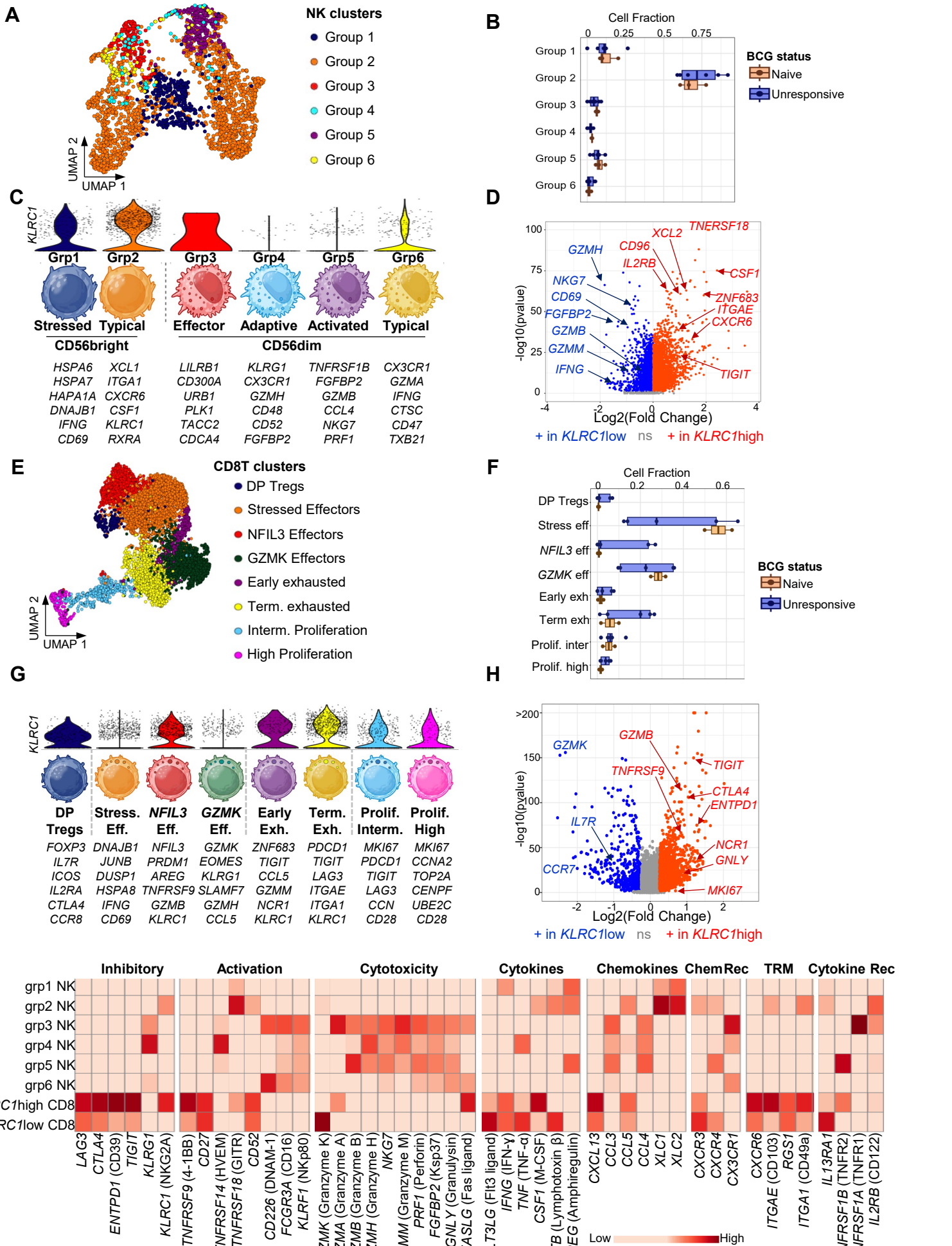

Figure 5

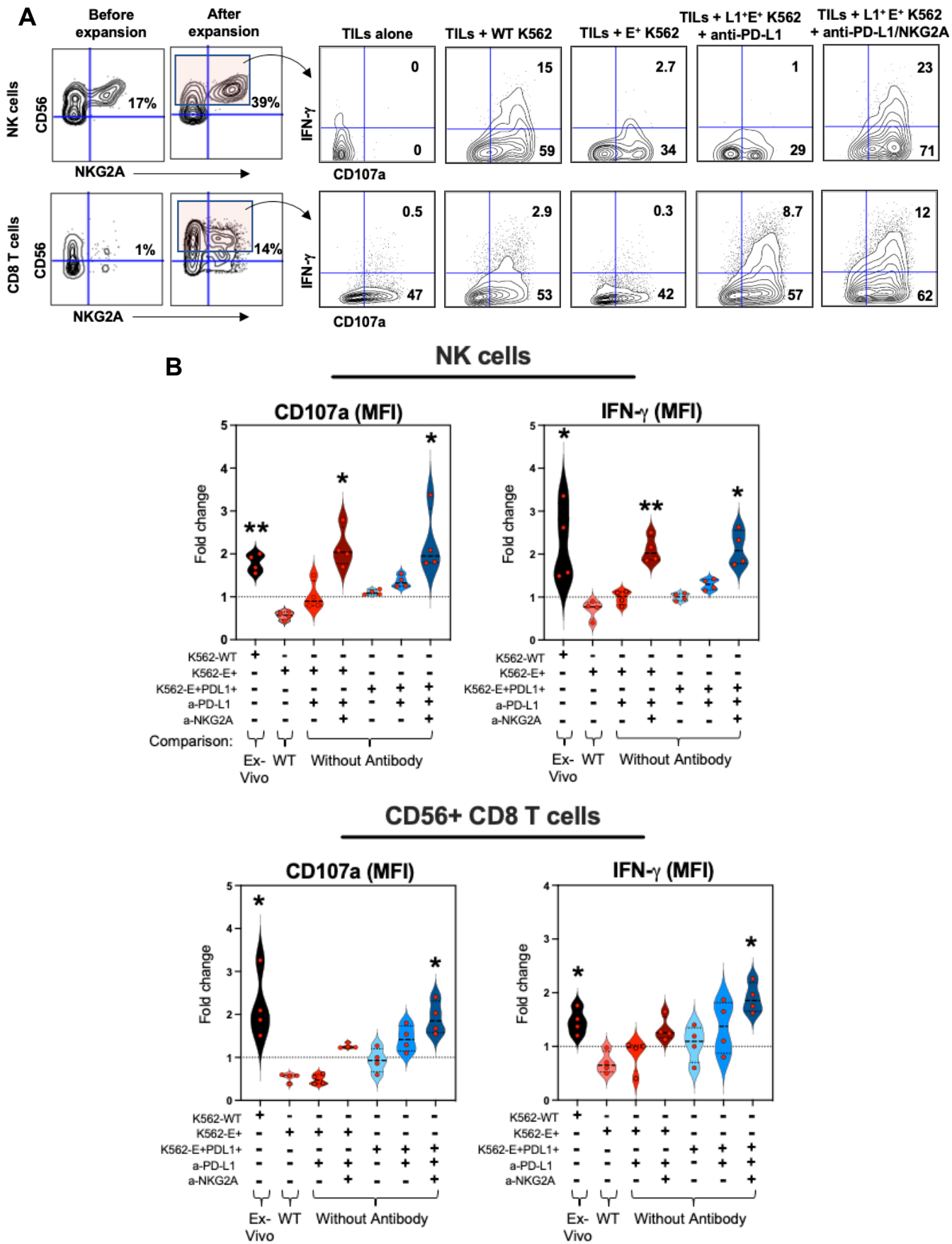

Figure 6